RESEARCH ARTICLE

Transition metal tungstates AWO_4 (A^{2+} = Fe, Co, Ni, and Cu) thin films and their photoelectrochemical behavior as photoanode for photocatalytic applications

Maria Joseíta dos Santos Costa[1] · Aline Estefany Brandão Lima[1] · Ester Pamponet Ribeiro[2] · Gilson dos Santos Costa[1] · Elson Longo[3] · Geraldo Eduardo da Luz Jr[1,2] · Laecio Santos Cavalcante[2] · Reginaldo da Silva Santos[1,2]

Abstract

This paper discusses about a facile transition metal tungstate thin films preparation method and their remarkable photoelectrochemical properties. The films of AWO_4 (A^{2+} = Fe, Co, Ni, Cu) were deposited onto conductive fluorine-doped tin oxide (FTO) glass substrate. The results of X-ray diffraction analysis indicated the presence of crystalline films. Field emission scanning electron microscopy images revealed nanostructured materials. X-ray photoelectron studies were employed to analyze elemental and chemical composition. Optical behavior indicated indirect transitions for all AWO_4 films. Photoelectrochemical studies displayed that AWO_4 films were successfully used as photoanodes in a photoelectrochemical cell under polychromatic irradiation. From electrochemical measurement, it was possible to estimate the flat band potential and so prevising suitable application of photoelectrodes. This work reports for the first time a comparative and comprehensive photoelectrochemical study with AWO_4 films prepared in a simple way. The results indicate that the films can be used as photoanodes in water splitting reactions and other photoelectrocatalytic applications.

✉ Laecio Santos Cavalcante
laeciosc@gmail.com

1   Programa de Pós-Graduação em Química-PPGQ,
    Universidade Federal do Piauí-UFPI, Teresina,
    PI 64049-550, Brazil

2   PPGQ-GreeTec-CETEM, Universidade Estadual
    do Piauí-UESPI, Rua: João Cabral, N, 2231, P.O. Box 381,
    Teresina, PI 64002-150, Brazil

3   CDMF, Universidade Federal de São Carlos-UFSCar,
    P.O. Box 676, São Carlos, SP 13565-905, Brazil

Graphical Abstract
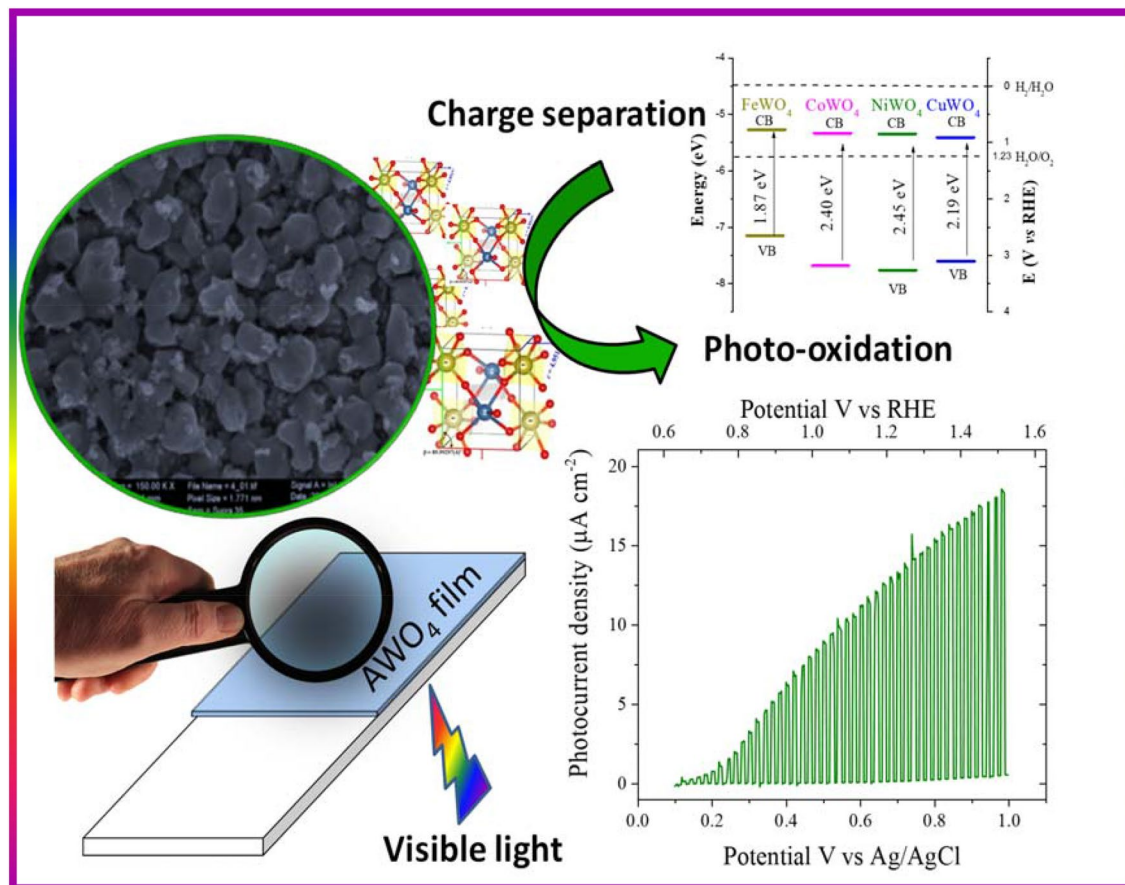
1 Introduction

In the last years, the growth of the world population and expansion of industrial centers have raised serious concerns caused by pollution and demands for clean water (H_2O) and energy [1]. Versatile, low-cost, and environment-friendly treatment technologies have been investigated to mitigate these issues. Besides that, recent developments in research and application of heterogeneous photocatalysis for light (ultraviolet, visible, or solar irradiation) conversion have been used as the most advanced and greenest method [2]. Among various semiconductors applications, photoelectrochemical (PEC) cell for H_2O splitting based on semiconductor oxides materials is a promising and environmentally friendly alternative approach to convert solar energy into a fuel source [3]. In addition, persistent organic pollutants or carbon dioxide (CO_2) can be converted into less inert compounds by photo(electro)catalytic processes [4].

In the photoelectrocatalysis process, the semiconductor material must be supported on the conductive substrate as a film, usually called photoelectrode. The photocatalytic process starts when the material absorbs light with energy equal to or superior to the semiconductor bandgap energy (E_{bg}) value [5]. This process results in photogenerated electrons ($e^-_{(CB)}$) in the conduction band (CB) and holes ($h^+_{(VB)}$) in the valence band (VB). These photogenerated charges can reach the semiconductor surface and then react with chemical species present in an electrolyte solution. It is typically considered that an electron can be transferred to an acceptor molecule if its redox potential lies below the CB of the photocatalyst, while a hole can be transferred to a donor molecule if its redox potential lies above the VB of the photocatalyst [6, 7].

Several types of metal oxide semiconductors such as titanium dioxide (TiO_2) [8, 9], tungsten trioxide (WO_3) [10], hematite (α-Fe_2O_3) [11], and zinc oxide (ZnO) [12], have been investigated in many photocatalytic applications. However, although these materials exhibit substantial photocatalytic activity, TiO_2 and ZnO have limited application due to their high E_{bg} values. On the other hand,

WO$_3$, α-Fe$_2$O$_3$ and Ag$_3$PO$_4$ oxides are colored, but have some drawbacks, which include reduced chemical stability at alkaline condition, acid medium and weak photostability, respectively [10–14]. In general, colored semiconductor oxides undergo photocorrosion, while white oxides like TiO$_2$ and ZnO are photoactive only under ultraviolet radiation. In addition, the main disadvantages presented by oxides in catalytic applications include a short carrier path length and, high charge carrier recombination [15–17]. Thus, ideally, it would be important to obtain oxides materials that present excellent chemical stability and photoactivity under visible irradiation. This way, it is important to research semiconductors with small E$_{bg}$, facile surface reaction kinetic, abundant and stable chemically semiconductors for efficient PEC H$_2$O splitting. Recently, our research group has investigated the properties of copper tungstate (CuWO$_4$) films as photoelectrode for photocatalysis applications [18, 19]. CuWO$_4$ is a transition metal tungstate, displays great chemical stability, and can harvest sunlight owing to its low bandgap energy.

Transition metal tungstates like AWO$_4$ (with A^{2+} = Fe, Co, Ni, and Cu) are ternary oxide semiconductors that have attracted considerable attention due to their interesting photoelectrochemical, electrocatalytic, luminescent, and photocatalytic properties [20, 21] Wolframite-type tungstates are favored by metal cations with radii less than 0.077 nm, while metal ions greater than 0.099 nm favor scheelite-type tungstates [22]. In tungstates with the wolframite-type monoclinic structure the transition metal (A) and W atoms are both bonded with six oxygen atoms to form [AO$_6$]/[WO$_6$] clusters. In scheelite structures, the transition metal is combined with eight oxygen and the W atoms are bonded with four oxygen, which forms the [AO$_8$]/[WO$_4$] clusters [23–25].

The iron tungstate (FeWO$_4$) is a semiconductor with a bandgap of approximately varying of 1.8 to 2.0 eV, absolving a wide range of light responses and playing an important role in the magnetic and photocatalytic potential application [26–28]. Cobalt tungstate (CoWO$_4$) has a well-defined magnetic structure and bandgap of about 2.8 eV, exhibiting excellent electrical and magnetic properties [29]. Nickel tungstate (NiWO$_4$) demonstrates an indirect bandgap of 2.0 eV [30] and the remarkable quantum size effect [31], which make it a potential photoanode candidate in the H$_2$O splitting; and, others applications including photocatalysis [32], antimicrobial [33] and electrocatalysis [34]. Copper tungstate (CuWO$_4$) has an indirect bandgap energy (E$_{bg}$) in the range of 2.2 to 2.45 eV [35–37], owing to their sufficient chemical stability, efficient sunlight utilization, and nontoxicity has seen applicated highly photoelectrocatalytic activity and photoelectrochemical H$_2$O splitting [38–40]. In addition, others applications have aroused technological and scientific interest such as scintillation detectors [41],

humidity and gas sensors [42, 43], supercapacitors [44], photoanodes [35], supercapacitor [45, 46], photoelectrolysis electrodes for lithium-ion batteries [47–49], electrochromic devices [44, 50] and photoelectrodes for hydrogen treatment [51].

Recently, some synthesis methods were employed for obtention of metal tungstate-based photoanode films as hydrothermal method [40], template-assisted synthesis method [52], co-precipitation [20], spray pyrolysis [53] and electrochemical deposition [54]. The polymeric precursor's method (PPM) has been very effective about conventional methods principally for wastewater treatment [55]. The main advantages of PPM have been seen allowing the control of the composition, the grain size, and the homogeneity of powders [56]. There is a variety of studies using AWO$_4$ as dispersed photocatalyst particles in the reaction medium for organic pollutants degradation. However, there are still few reports of preparing films from these materials. In addition, most film preparation methods are time-consuming and require an expensive structure. Thus, simple methodology, low cost, and high-performance AWO$_4$ films still need to be investigated. To the best of our knowledge, the PPM has not been used to obtain transition metal tungstate AWO$_4$ (A^{2+} = Fe, Co, Ni, and Cu) thin films. PPM has been studied in preparation of AWO$_4$ oxides semicondutores at powder form. In addition, this is the first time that a detailed photoelectrochemical study of these materials has been presented.

Therefore, in this paper, AWO$_4$ (A^{2+} = Fe, Co, Ni, and Cu) thin films were synthesized by the PPM and deposited on the transparent conductive substrate (FTO-glass) using a simple drop-casting method. After thermal treatment, the film's photoelectrochemical behaviors were investigated. These studies are important and can provide information about the potential use of films in photocatalytic applications, such as H$_2$O splitting. Besides, all films were structurally characterized using X-ray diffraction (XRD) patterns; the composition was analyzed by X-ray photoelectron spectroscopy (XPS); the morphological features were examined by field emission scanning electron microscope (FE-SEM), and the optical bandgap energies were estimated using UV–Vis spectroscopy.

2 Experimental section

2.1 Materials and procedure

The citric acid (C$_6$H$_8$O$_7$; 99% purity), tungstic acid (H$_2$WO$_4$; 99% purity), ammonium iron (II) sulfate hexahydrate [(NH$_4$)$_2$Fe(SO$_4$)$_2$, 99,9% purity], cobalt (II) nitrate hexahydrate [Co(NO$_3$)$_2$·6H$_2$O, 99.99% purity], nickel (II) nitrate hexahydrate [Ni(NO$_3$)$_2$·6H$_2$O, 99.99% purity] and copper nitrate trihydrate [Cu(NO$_3$)$_2$.3H$_2$O; 99% purity] were

purchased from Sigma-Aldrich®. Ammonium hydroxide (NH_4OH, 35% purity) and ethylene glycol ($C_2H_6O_2$, 99.5% purity) were purchased from Dynamic®.

AWO_4 (A^{2+} = Fe, Co, Ni, Cu) films were obtained from the resin by thePPM [57]. This is a modified sol–gel method that is based on the complexation of metal alkoxides, and the esterification/polymerization reaction [58]. Recently, this synthesis method has been successfully used to obtain crystalline ceramic powders when calcined at temperatures between 500 and 700 °C [55, 59, 60]. For first time here was used to obtain metal tungstate thin films.

2.2 Synthesis of AWO_4 thin film by polymeric precursor method

A tungsten metal citrate (Cit-W, pH = 7) was initially prepared using deionized water (DI-H_2O) as a solvent, 0.135 mol citric acid ($C_6H_8O_7$) as a complexing agent and 0.045 mol tungstic acid (H_2WO_4) as a network modifier forming a transparent solution with concentration of 0.4256 µmol L^{-1}. After homogenization, bivalent cation precursors ($A = Fe^{2+}$, Co^{2+}, Ni^{2+}, and Cu^{2+}) were added to citrate, respectively. The 150 g citrate with each bivalent cations was heat-treated and stirred at 90 °C for 2 h and obtained a homogeneous brown, wine, green, and blue color solution for iron, cobalt, nickel, and copper, respectively. Ammonium hydroxide (NH_4OH) was used to adjust the pH ~ 7. This solution was polymerized with the addition of 2.467 g ethylene glycol ($C_2H_6O_2$, polyalcohol); after reaction at a temperature of approximately 90 °C is formed a polyester and H_2O. The citric acid/metal molar ratio was set at 3:1 and 60:40 for citric acid/ethylene glycol to promote citrate polymerization. The polymerized solution was heated until H_2O evaporated and a polymeric resin formed about 24 h and cooled to 16 °C. Before the film's preparation, the FTO glasses (1.0 × 2.5 cm) were cleaned by a sonication bath, successively, with H_2O and a neutral liquid soap, DI–H_2O, and finally with isopropyl alcohol for 15 min in each step. For films preparation, an adhesive tape was used to define the geometrical area of the films (1.0 cm^2); then, 80 µL resin was dripped onto the FTO-glass (Sigma-Aldrich® R-7Ω cm^{-2}) by dropping casting method, heated at 100 °C for 1 h (10 °C /min) and heat-treated at 500 °C for 2 h (2 °C /min) in a muffle furnace. To form a second and third layer, the resin was dropped again, heated and one unique thermal treatment was realized.

2.3 Structural, morphological, optical, and composition characterization of AWO_4 films

AWO_4 ($A = Fe^{2+}$, Co^{2+}, Ni^{2+}, and Cu^{2+}) thin films were characterized by the X-ray diffraction (XRD)

pattern (Rigaku-DMax 2500PC, Japan with Cu Kα radiation ($\lambda = 0.15406$ nm) in the 2θ range from 10 to 80° with a scan speed of 0.02°/min. The diffraction patterns were compared to the data from the Inorganic Crystal Structure Database (*ICSD*). Optical analyzes were obtained by UV–Vis transmittance spectra using the UV–Vis spectrophotometer (Shimadzu, 2600). The E_{bg} values of the samples was obtained by the transmittance spectrum in the UV–Vis region, using FTO-glass as a reference, applying the Wood-Tauc plot method [61]. The surface and average grain size were characterized by field emission–scanning electron microscopy (FE-SEM, Supra 35-VP Carl Zeiss (Germany)). The images were obtained with a working voltage of 15 kV. The composition of the heterojunction film surface was analyzed by X-ray photoelectron spectroscopy (XPS; Scientia Omicron ESCA, Germany) using a monochromatic X-ray Al Kα (1486.7 eV).

2.4 Photoelectrochemical analysis of AWO_4 photoelectrodes

The photoelectrochemical properties were investigated using an electrochemical cell fabricated with an optic glass window (100% transmittance for $\lambda > 360$ nm). Working electrodes were the AWO_4 (A^{2+} = Fe, Co, Ni, and Cu) films, a Pt wire as the counter electrode, and Ag/AgCl (in 3.0 mol L^{-1} KCl saturated aqueous solution) was the reference electrode (in Luggin capillary). A three-electrode system configuration was used to measure; and so, was investigated in an aqueous solution of 0.1 mol L^{-1} Na_2SO_4 (pH 5.6) as the inert support electrolyte.

The measurements were performed using an Autolab Potentiostat/Galvanostat (PGSTAT302N Metrohm) and recorded by the NOVA 1.7 software, in the absence of light (dark) and under backside polychromatic irradiation. A metallic vapor discharge lamp (HQI-TS NDL) with a nominal potency of 150 W was used to irradiate the system. All our measurements were carried out with an irradiance of 100 mW cm^{-2}, with the AWO_4 films placed 10 cm from the irradiation source, similar to previous studies carried out by our group [9, 62]. The irradiance was measured with a Newport Power Meter, model 843-R. For more details on the behavior of the radiation source, see the supplementary material section (Fig. S1). Photoelectrochemical analyses consisted initially in the determination of layers which were using linear sweep voltammetry (LSV). Thus, the determination of the flat band potential (E_{fb}) was carried out with the data recorded in the anodic potential range of 0.1–1.3 V at a scan rate of 1.0 mV s^{-1}, using a chopped illumination at 0.1 Hz following the Gärtner–Butler model [63, 64].

The photocurrent-potential was measured using cyclic voltammetry (CV) with a scan rate of 20 mV/s in the dark and under polychromatic irradiation. Also, the chronoamperometric curves were registered under dark or light conditions with the electrodes polarized at +0.7 V (vs Ag/AgCl). For comparison, the potential registered using the Ag/AgCl reference electrode was adjusted to a reversible hydrogen electrode (RHE), according to the Eq. (1) [37, 54, 65]:

$$E \text{ (vs. RHE)} = E \text{ (vs. Ag/AgCl)} + 0.0591 \text{Vx pH} + 0.199 \text{V}. \tag{1}$$

Further, the potentials after adjustment with respect to the RHE (in volts) were converted to energy levels (eV) relative to vacuum level using Eq. (2) [66]:

$$E_{(eV)} = \left[-4.5 \text{eV} - eE_{(RHE)} \right] \tag{2}$$

From the photoresponse, it was possible to calculate the recombination lifetime from the time constant (τ) obtained from Eq. (3), which describes the kinetics of the transient currents as follows below:

$$R = \exp(-t/\tau) \tag{3}$$

where the ratio R is $R = \frac{J_t - J_{st}}{J_{in} - J_{st}}$, J_t is the photocurrent at time t, J_{st} is the steady-state photocurrent, and J_{in} is the photocurrent at the initial time [67, 68].

3 Results and discussion

3.1 Structural, morphological and optical characterization of AWO_4 films

The crystal structures of the resulting samples were identified by the X-ray diffraction (XRD) patterns. The XRD patterns are recorded in the range of 10–80º as shown in Fig. 1a–d. Diffraction signals suppressed and marked with the symbol "•" correspond to the FTO transparent conductive glass substrate.

For $FeWO_4$, $CoWO_4$, and $NiWO_4$ films displayed in Fig. 1a–c, the XRD patterns show diffraction peaks which are characteristic and attributed to (010), (100), (110), (011), (111), ($\overline{11}$ 1), (020), (002), (021), and (200) planes, at 2θ equal to 15.6º, 19º, 24º, 25º, 30.6°, 31°, 36°, 37°, and 38°, respectively. These XRD patterns are characteristic of wolframite-type monoclinic phase structure with space group ($P2/c$) as determined by $ICSD$ card No. 15952, 15851, and 15852 for $FeWO_4$, $CoWO_4$, and $NiWO_4$ crystal, respectively [69, 70]. On the other hand, the XRD pattern for the $CuWO_4$ sample (Fig. 1)d shows typical diffraction peaks for triclinic structure ($ICSD$ No. 16009) with space group ($P\overline{1}$) [71]. The XRD diffraction were registered at 2θ of 15.29º, 18.19º, 19.02º, 22.94º, 23.56º, 24.13º, 25.96º, 26.97º, 28.70º, 30.14º, 30.85º,

Fig. 1 XRD patterns of (**a**) $FeWO_4$, (**b**) $CoWO_4$, (**c**) $NiWO_4$, and (**d**) $CuWO_4$ thin films synthesized by the PPM and heated at 500 °C for 2 h. The "•" indicates the FTO-glass substrate. The vertical bars represent planes and intensity of the $ICSD$ card No. 15952, 15851, 15852, and 16009 for the pure monoclinic $FeWO_4$, $CoWO_4$, $NiWO_4$ phase, and pure triclinic $CuWO_4$ phase, respectively
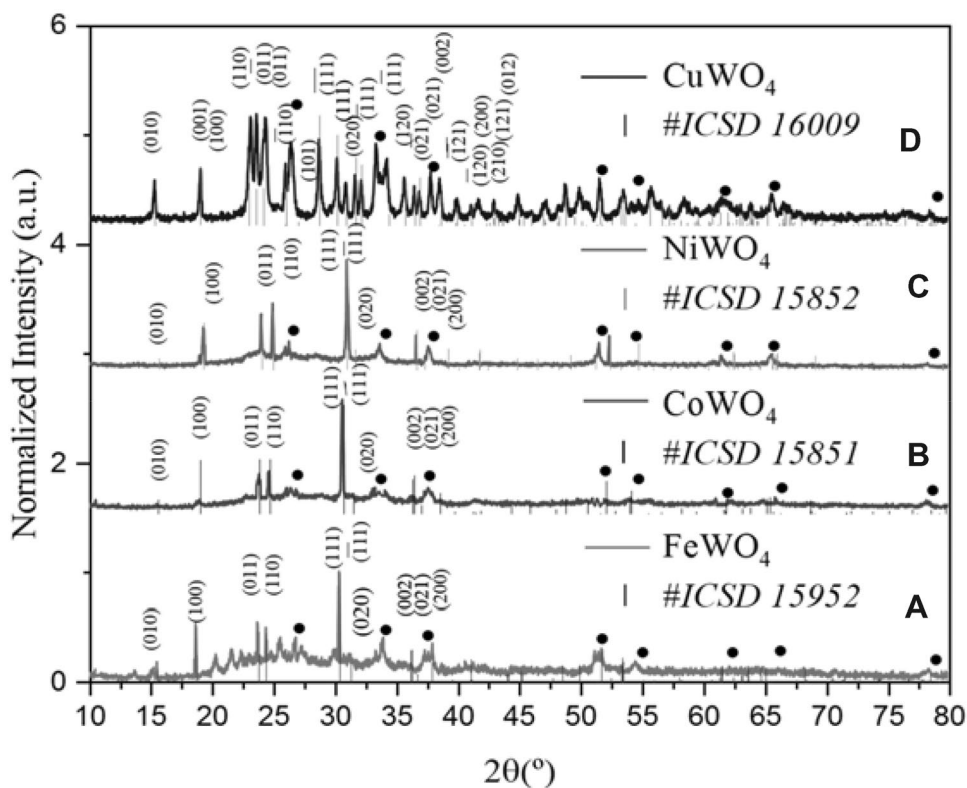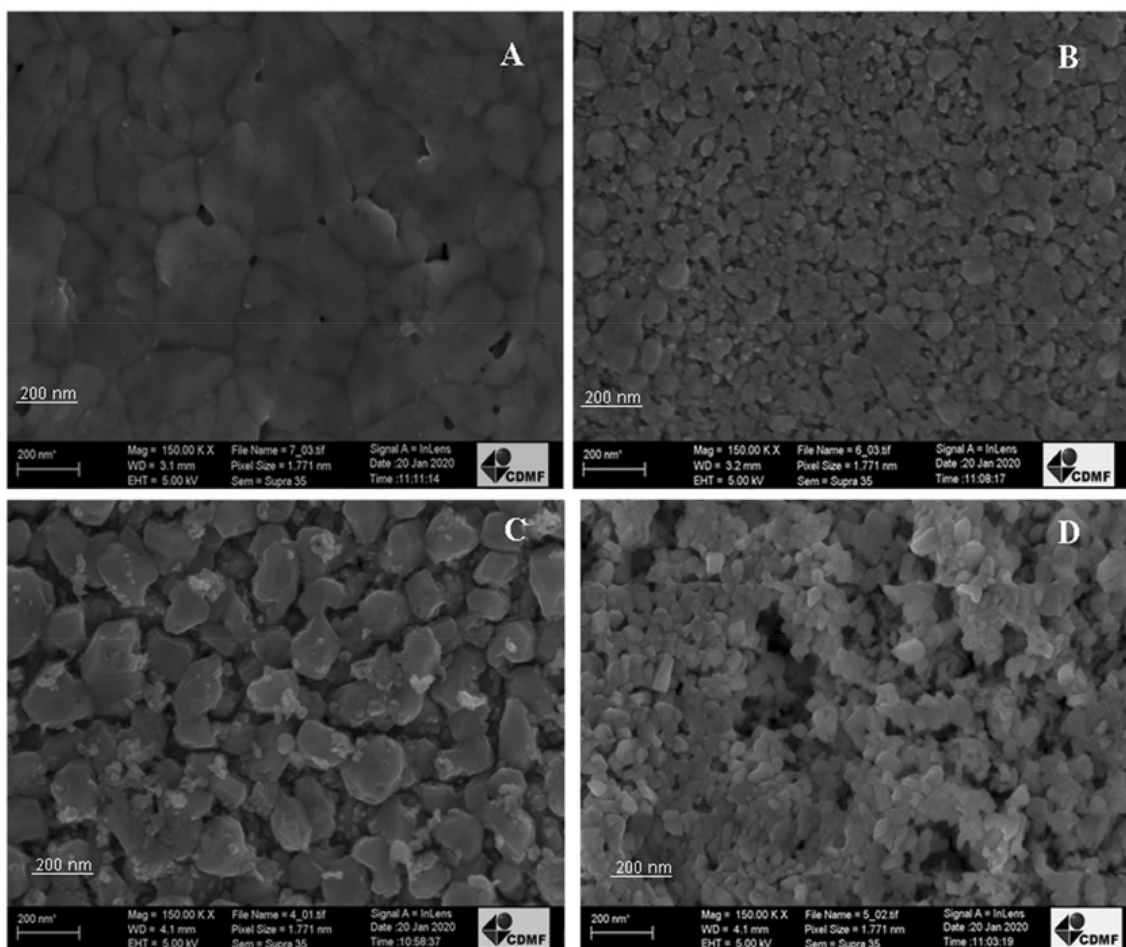
Fig. 2 FE-SEM images of the surface of the (**a**) FeWO$_4$, (**b**) CoWO$_4$, (**c**) NiWO$_4$, (**d**) and CuWO$_4$ films synthesized by PPM and heated at 500 °C for 2 h

31.65°, 32.11°, 34.34°, 35.66°, 36.44° and 36.86°, which correspond to the planes (010), (001), (100), (110), (0 $\bar{1}$ 1), (011), ($\bar{1}$ 10), (101),($\overline{11}$ 1), (111), (020), ($\bar{1}$ 11), (1 $\bar{1}$ 1), (120), (0$\bar{2}$1), (021), and (002), respectively. The diffraction peaks without other impurities or deleterious phases, which suggests that films can be prepared successfully by means of PPM.

FE-SEM images for the morphology, particles size, and surface of AWO$_4$ (A^{2+} = Fe, Co, Ni, and Cu) films are shown in Fig. 2a–d, respectively. In Fig. 2a–d, the FE-SEM images revealed the morphology and particles size of the FeWO$_4$, CoWO$_4$, NiWO$_4$ and CuWO$_4$ films. The deposition of the FeWO$_4$, CoWO$_4$, NiWO$_4$, and CuWO$_4$ films on a conductive substrate (FTO-glass), followed by annealing at 500 °C, led to an immobilized particle density of ca. 1.6 ± 0.2 mg cm^{-2}, 1.2 ± 0.2 mg cm^{-2}, 0.9 ± 0.2 mg cm^{-2} and 1.4 ± 0.1 mg cm^{-2}, respectively. The FeWO$_4$ film presented in Fig. 2a indicates that has a well-sintered nanoplates-like structure with an average particles size of 51.3 nm $\pm$ 1.343 (See histogram in Fig. S2(a)). Yu et al. reported that FeWO$_4$ synthesized

by hydrothermal method present morphology influenced by pH condition, which can change from hexagonal flakes to nano-rods [72]. Figure 2b shows the morphological surface for CoWO$_4$ film with irregular spherical nanoparticles and an average particles size of ca. 27.7 nm $\pm$ 0.9799 (See histogram in Fig. S2(b)). Whereas, the NiWO$_4$ film exhibits an irregular surface morphology formed by polyhedron interconnected particles (Fig. 2c) and an average particles size of ca. 74.75 nm $\pm$ 0.8185 (See histogram in Fig. S2(c)). Figure 2d shows that CuWO$_4$ film is formed by irregular nanoparticles with an average size of 24.77 nm $\pm$ 2.537 (See histogram in Fig. S2(d)). Thus, the presence of several grains in the CuWO$_4$ film agglomerated is very similar to that spectated to triclinic structure crystals [37]. In this case, a porous structure with a non-uniform pore distribution is formed. This porous nanostructure can contribute to superior charge mobility and a large specific surface area [73]. In all cases, the average crystal size was calculated by equatorial diameter and estimated using the GNU Image Manipulation Program (GIMP 2.10.10 version for Windows 7–64 bits) [74].
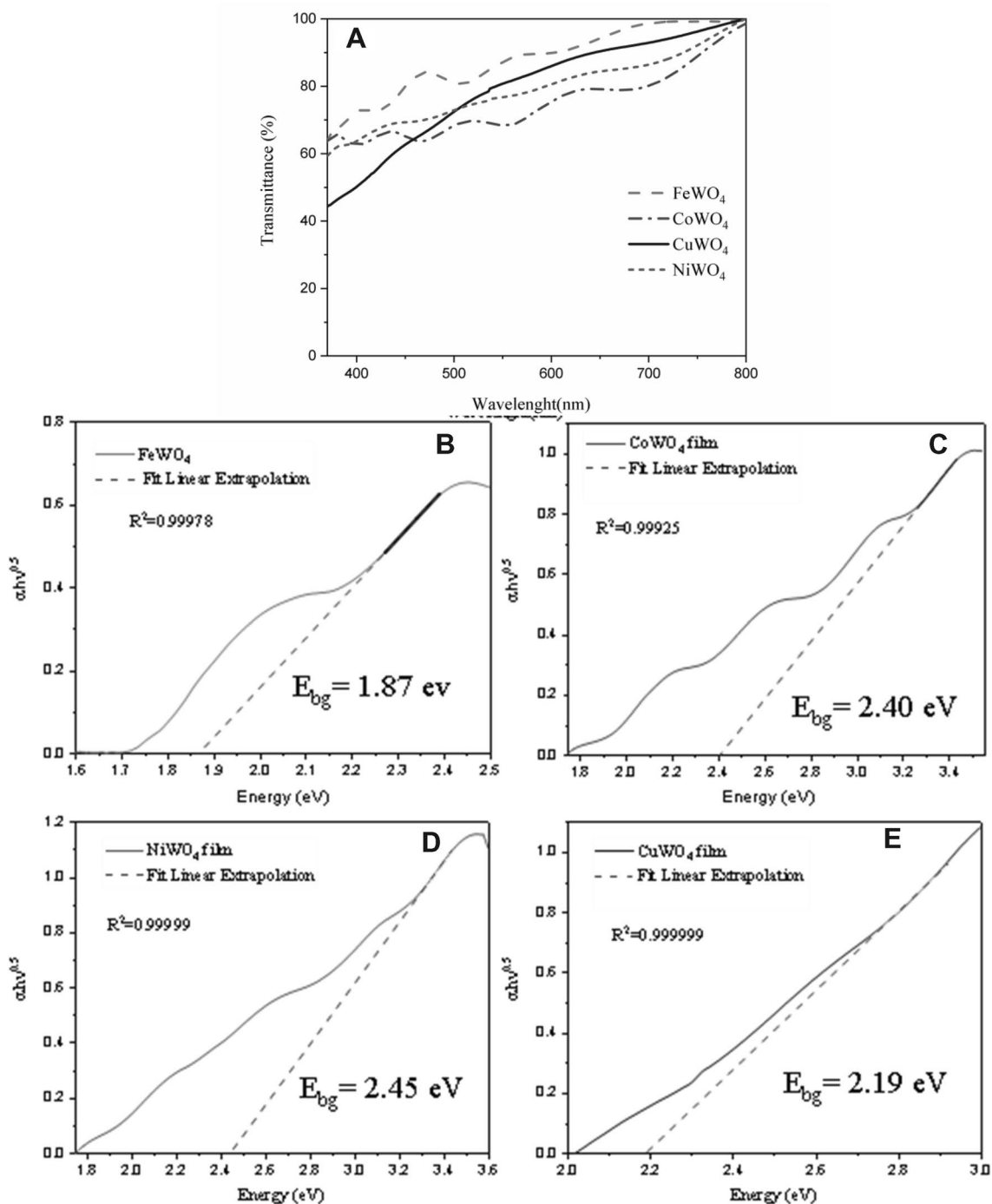
Fig. 3 **a** UV-Vis transmittance curves of films and bandgap energy estimated by Wood-Tauc plot method for (**b**) FeWO$_4$, (**c**) CoWO$_4$, (**d**) NiWO$_4$ and (**e**) CuWO$_4$ film deposited on FTO substrate.

The optical properties of these films were examined with UV–Vis spectra registered in transmittance mode and estimated the bandgap energy (E_{bg}) by Wood-Tauc plot method as shown in Fig. 3. Figure 3a shows that the AWO$_4$ (A^{2+} = Fe, Co, Ni, and Cu) films had a maximum transmittance of ~72% in the visible region and interference fringes

can be registered in FeWO$_4$, and CoWO$_4$ thin films. Considering an indirect gap transition, the optical E_{bg} for AWO$_4$ (A^{2+} = Fe, Co, Ni, and Cu) films were calculated with the following Eq. (4) [61]:

$$(\alpha h\upsilon)^{0.5} = C(h\upsilon - E_{bg}). \qquad (4)$$

In this Eq. (4), the $h\upsilon$ is the incident photon energy, C is a constant of proportionality of semiconductors, E_{bg} is the optical bandgap energy and α is the optical absorption coefficient of the film. According to the equation, $(\alpha h\upsilon)^{0.5}$ has a linear relation with the $h\upsilon$ [75]. The optical E_{bg} values of AWO_4 (A = Fe, Co, Ni, Cu) films were determined by extrapolation of the linear relation to $(\alpha h\upsilon)^{0.5} = 0$. As illustrated in Fig. 3 b–e, the E_{bg} of $FeWO_4$, $CoWO_4$, $NiWO_4$ and $CuWO_4$ films are estimated to be about 1.87, 2.40, 2.45, and 2.19 eV, respectively. These E_{bg} values are slightly close that on registered in other studies [30, 54, 76–80]. Slight deviations in the E_{bg} values can be attributed to the effects of film morphology and particle sizes. These results indicate that the materials are able to harvest sunlight. Also, UV–Vis measurements using an integrating sphere were made. In general, there are no significant differences for the curves registered in both modes (See Fig. S3 on the Supporting Information).

An X-ray photoelectron spectroscopy (XPS) analyses were utilized to investigate the elemental and chemical composition of samples, as shown in Figs. S4, and 4. A full survey spectrum shown in Fig. S4 indicate the presence of Fe 2p [81], Co 2p [82], Ni 2p [83], and Cu 2p states [51] signals due to presence these elements in $FeWO_4$, $CoWO_4$, $NiWO_4$, and $CuWO_4$ films samples. All XPS spectra are attributed to the constituent element core levels or Auger lines. Also, in all survey analyses, it was possible to observe the presence of corresponding peaks O 1 s and W 4f. The C 1 s peak can be attributed to carbon adsorbed on the surface of the AWO_4 films, probably due to polymeric precursors method not completely eliminated during the thermal treatment. Table S1 displays the values of XPS primary peak for all A divalent ions transitions metal (A^{2+} = Fe, Co, Ni, and Cu), W 4f, and O 1 s core-level binding energies.

Metal ions (A^{2+} = Fe, Co, Ni, and Cu) 2p state in XPS spectra of each AWO_4 film are presented in Fig. 4a–d. The deconvoluted Fe 2p XPS (Fig. 4)a consists of two peaks which corresponds the binding energy of Fe $2p_{3/2}$ (710.70 and 712.48 eV), which higher binding energy of 712.48 eV can be attributed to + 3 oxidation state [84], and Fe $2p_{1/2}$ (724.88 eV) due to Fe^{2+} in the lattice sites of $FeWO_4$ film [85]. In addition, there are two shake-up satellite peaks at Fe $2p_{3/2}$ (715.71 and 719.81 eV) and one satellite peak at Fe $2p_{1/2}$ (732.07 eV), which are typical Fe^{2+} oxidation states [86]. By using a Gaussian fitting method, the high-resolution Co 2p spectra is deconvoluted into two spin–orbit doublets and two shake-up satellites peaks (802.08 and 785.28 eV) [87]. The XPS Co 2p core-level spectra of $CoWO_4$ film is presented in Fig. 4b. The deconvolution of Co 2p peak is divided in Co $2p_{3/2}$ (779.94 and 781.31 eV) and Co $2p_{1/2}$

(796.57 eV) understanding Co^{2+} oxidation state. In same way that Fe for peaks of Co 2p (higher binding energy of 781.31 eV) attributed to + 3 oxidation state [88].

Similarly, an XPS Ni 2p spectrum of $NiWO_4$ film is seen in Fig. 4c. The binding energy of the Ni $2p_{3/2}$ (855.08 and 856.59 eV) and Ni $2p_{1/2}$ (872.66 and 874.28 eV) are resulted of spin–orbit doublets deconvolution which characteristic of Ni^{2+} and two shake-up satellite peaks (856.59 and 874.28 eV) and good agreement with the literature data [34]. Two deconvolution of Ni 2p (higher binding energy of 874.28 eV and 856.59 eV) can be attributed to + 3 oxidation state [89]. The satellites peaks are typical shake-up satellites which were due to the multielectron transitions and the decrease of the kinetic energy of emitted photoelectrons [90, 91]. Also, Fig. 4d shows XPS core-level spectrum of Cu 2p, which displays two sets of Gaussian doublets (Cu $2p_{3/2}$ and Cu $2p_{1/2}$) located at 931.33/933.61 eV, and 951.42/953.54 eV and shake-up satellite peaks located at 940.52, 942.80 and 961.40 eV assigned to a typical feature for Cu^{2+} oxidation state [92]. On the other hand, Tang and co-works have shown in previous works that signals which occur at lower binding energy values (951.42 and 931.33 eV) can be attributed to Cu^{1+} oxidation state [51]. The appearance of doublet peaks in bivalent cations can indicate presence of monovalent or trivalent cations (A^+ or A^{3+}) [91, 93]. Figure 4e displays the W 4f core-level spectra of AWO_4 (A^{2+} = Fe, Co, Ni, and Cu) films. The deconvolution of W 4f spectra into one pair of spin–orbit doublet peaks dominated by W $4f_{5/2}$ and W $4f_{7/2}$ states corresponding to the W^{6+} valence state in tungstate-based crystal structure [7, 94]. The binding energy values of W 4f show doublet of W $4f_{7/2}$ and W $4f_{5/2}$, besides W $5p_{3/2}$ at 33.64/34.28, 35.95/37.22 and 39.83 eV for $FeWO_4$, 34.26/34.96, 36.45/36.65 and 40.36 eV for $CoWO_4$, 34.14/34.72, 36.57/36.71 and 40.37 eV for $NiWO_4$ and 34.42/35.07, 36.73/37.91 and 40.19 eV for $CuWO_4$ [95]. The appearance of doublet peaks of W 4f and W5p in XPS spectra indicates the presence of W^{5+} in the film [96]. As the presence of W^{5+} (or A^+) in AWO_4 films can induce oxygen vacancies that are regarded as shallow donors [52], a higher concentration of W^{5+} will result in a larger electron density in metal tungstate-based films [51]. Figure 4f shows the XPS O 1s core-level spectra of AWO_4 films annealed at 500 °C for 2 h. The O1s spectra was decomposed into three peaks located at 529.89, 530.88 and 531.60 eV, and were assigned to the O–W–O bonds, lattice oxygen of Fe–O–Fe, metallic oxide of Fe–O bonds in $FeWO_4$, respectively [2, 26]. Similarly, the XPS O 1s spectra of $CoWO_4$ was analyzed and then, was observed three peaks located at 529.32, 530.23 and 531.40 eV. For $NiWO_4$, the O 1s core-level spectra deconvoluted into three peaks are located at 529.46, 530.27, and 531.57 eV. Similar to others films, the O 1s core-level spectra of $CuWO_4$ was also deconvoluted in three peaks located at 529.76, 530.56 and 531.65 eV corresponding to same
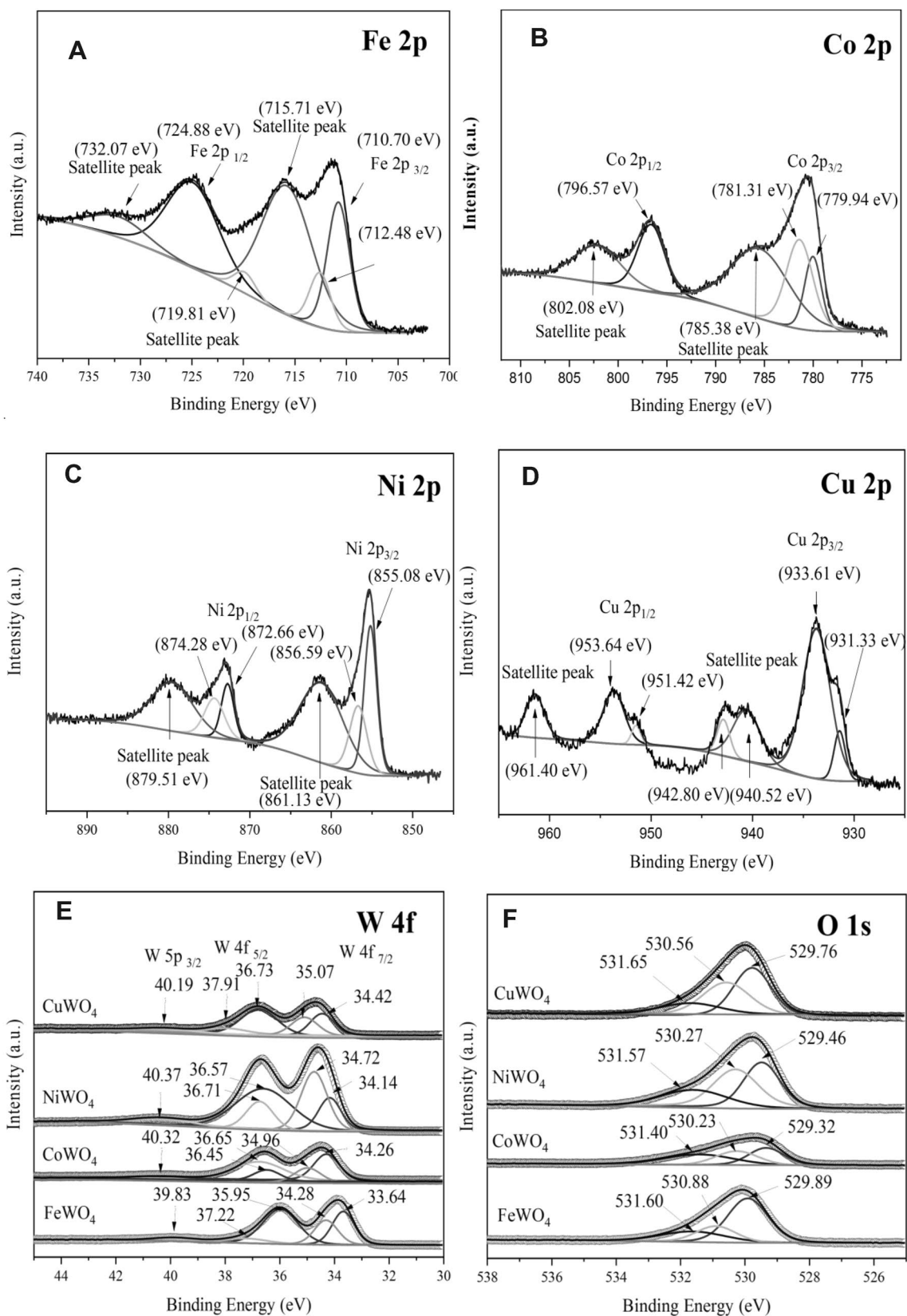
Fig. 4 High—resolution XPS spectra for (**a**) Fe 2p, (**b**) Co 2p, (**c**) Ni 2p, (**d**) Cu 2p, (**e**) W 4f, and (**f**) O 1 s core-level spectra of FeWO$_4$, CoWO$_4$, NiWO$_4$, and CuWO$_4$ film, respectively
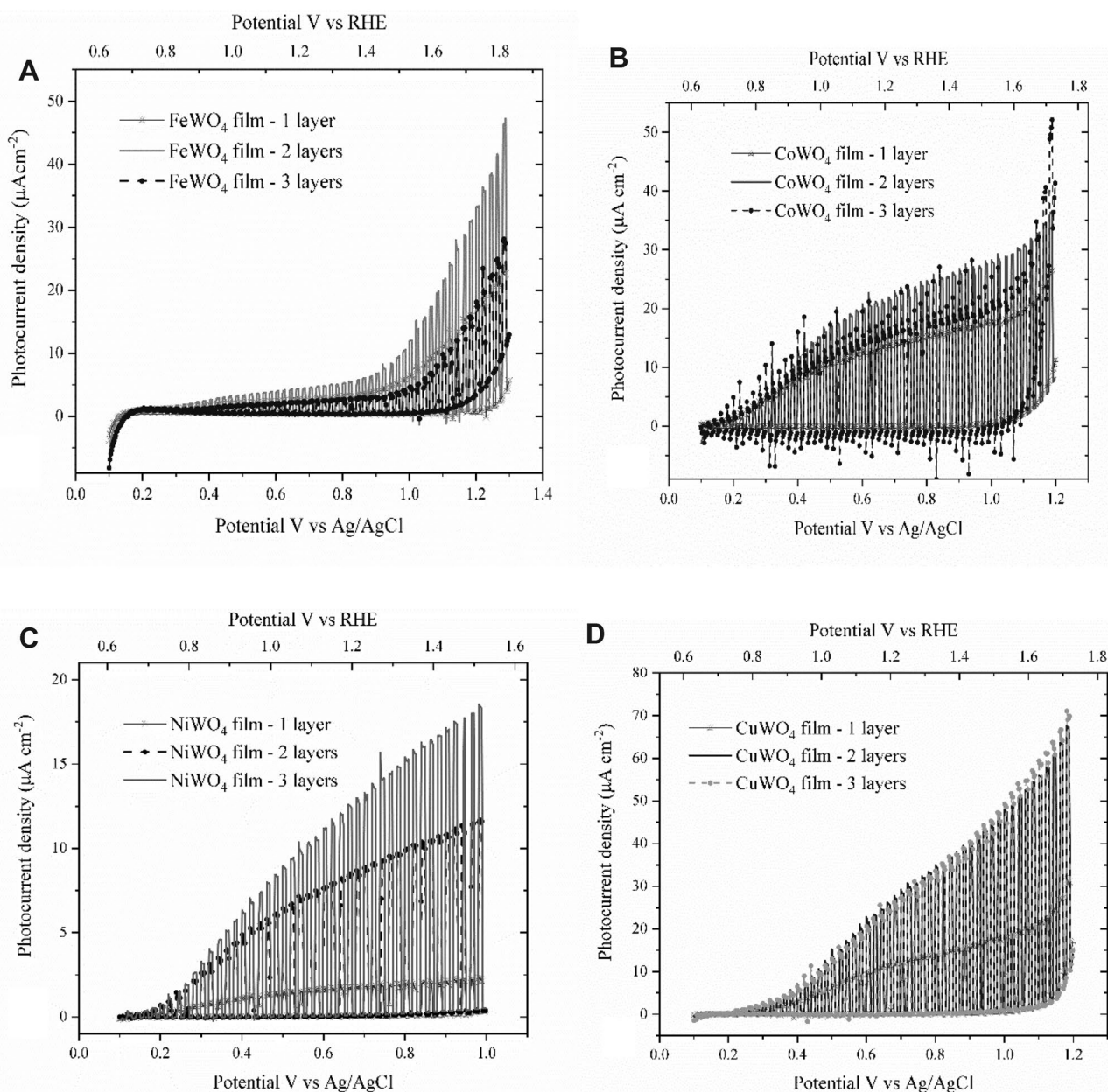
Fig. 5 LSV curves plots of (**a**) FeWO$_4$, (**b**) CoWO$_4$, (**c**) NiWO$_4$, and (**d**) CuWO$_4$ photoanodes in inert 0.1 mol L^{-1} Na$_2$SO$_4$ solution (pH ~ 5.6) irradiated with chopped polychromatic light (0.1 Hz), respectively

description as previously presented. The XPS spectra confirm the formation of possible defect states on the surface and suggest the presence of oxygen vacancies created during production and incorporated in the crystal analyzed [15]. Here, the XPS data suggest that oxygen vacancies cause lower oxidation states in metals, in order to maintain the electroneutrality of the material. Thus, these defects may be responsible for the *n*-type conductivity of semiconductors, as well as the non-stoichiometry at surface FeWO$_4$, CoWO$_4$,

NiWO$_4$, and CuWO$_4$ films [97]. Hence, the XPS spectra confirm the formation of good-quality tungstate-based films.

3.2 Photoelectrochemical behavior of *A*WO$_4$ films

Figures 5a–d show the photoelectrochemical behavior of *A*WO$_4$ (*A*$^{2+}$ = Fe, Co, Ni, and Cu) films with different deposited layers on FTO-glass was examined by linear sweep voltammetry (LSV) curves registered at 1 mV s^{-1} under chopped 0.10 Hz polychromatic irradiation. All *A*WO$_4$ films

displayed a more negative photo-potential after irradiation condition, which means, in the dark the open-circuit-potential (OCP) value is more positive than OCP registered under irradiation condition ($E_{light-on} < E_{light-off}$ vs. Ag/AgCl). This negative photo-potential is characteristic of n-type semiconductor oxides [98]. Thus, LSV curves were registered toward anodic direction and positive photocurrents were observed as applied bias until oxygen evolution reaction (OER) signals under dark condition. To investigate the influence of AWO_4 film layers on photocurrent response, samples were prepared with one, two, and three layers.

For $FeWO_4$ and $CoWO_4$ materials, films with two layers showed the best photoresponse values, which can be with associated adequate quantity and thickness of semiconductors, as shown in Fig. 5a,b. Moreover, the $FeWO_4$ and $CoWO_4$ films with three layers showed lower values of photocurrents, suggesting that these films present greater resistance in the flow of electrons. From Fig. 5c,d, it is possible to observe that this reduction in photocurrents values was not registered for $NiWO_4$, and $CuWO_4$ films. In $NiWO_4$ film with three layers, higher photocurrents were observed, while in $CuWO_4$ films this photoresponse value was maintained. For comparison effect, all other photoelectrochemical measures registered hereinafter were developed with two layers for $FeWO_4$, $CoWO_4$, $NiWO_4$, and $CuWO_4$ films.

From Fig. 5a, it is possible to observe that an enhancement in photocurrent density of $FeWO_4$ photoelectrode started from 0.95 V vs. Ag/AgCl (1.48 V vs. RHE). For $CoWO_4$, $NiWO_4$, and $CuWO_4$ the photocurrent values evolve in potentials closer to OCP, suggesting that in these films the electrons can reach the conductive substrate more easily. In all photoelectrodes, some positive spikes of current were observed immediately after the light was turned on, followed by an exponential drop in current values, which can be related to transient effects in the semiconductor material [65]. These spikes can be caused by the rapid injection of electrons into the CB (peak anode current), while the exponential drop is related to the electron/hole charges recombination process, even under polarization conditions. When the light is turned off, rapid recombination in VB happened and cathodic spikes can be registered, as displayed in Fig. 5b [99]. Current spike behavior also depends on the degree of crystallinity. Current spike diminishes by increasing the annealing temperature, but the conductivity of FTO substrate deteriorates at temperature above 500 °C. The $NiWO_4$ shows a beautiful LSV curve (Fig. 5c) due to a good crystallinity as shown in FE-SEM (Fig. 2c) and large particle size (Fig. S2c). Also, this transient cathodic peak can be associated to back electron transfer from the external circuit to the photoanode, which resulted in a surface recombination process [100]. According to Le Chatelier's principle, a system at equilibrium that is subjected to an alteration in concentration will readjust itself to counteract

the alteration and establish a new equilibrium caused by an excess of electrons. This would explain the transient current spikes in the AWO_4 photoanodes.

The photocurrent density measurements by LSV curves were utilized to estimate the flat band potential (E_{fb}) of these semiconductors, following the Butler-Gärtner model [63, 64], as displayed in Fig. 6(a–d). Gärtner–Butler analysis is an alternative method of determining the E_{fb} is based on the measurement of the square of the photocurrent density as a function of electrode potential. The E_{fb} is predicted to be at the intercept of the square of the photocurrent density with the potential axis [101]. This model assumes that the photocurrent (I_{ph}) is observed only when the electrode potential is more positive than the semiconductor flat band potential (i.e., when $E > E_{fb}$ and $I_{ph} > 0$). Thus, the Butler-Gärtner model can be represented by Eq. (5) below:

$$I_{ph} = \alpha W_0 q \varphi_0 \sqrt{E - E_{fb}} \tag{5}$$

where α is the absorption coefficient, W_0 is the depletion layer width, φ_0 is the radiation intensity, q is the electron charge, and E_{fb} is the flat band energy. This methodology already was employed to determine E_{fb} values for other photoelectrodes by our research group [11, 37, 102]. Therefore, E_{fb} values obtained by extrapolation of photocurrent initial potential were estimated at 0.23, 0.25, 0.28, and 0.38 V (vs. Ag/AgCl) for $FeWO_4$, $CoWO_4$, $NiWO_4$, and $CuWO_4$ electrodes, respectively. The E_{fb} value is strongly dependent on the medium conditions such as pH and electrolyte composition, as well as film thickness, crystal structure, and morphology of the semiconductor [103]. It is very important to determine the E_{fb} value of semiconductor materials before its application in any photoelectrochemical proposition [97, 104–106], since this electrode potential can be related to the Fermi energy level and the CB band edge position in n-type semiconductors [107]. The flat band potential and CB must be related to electron donor and acceptor states using Eq. (6):

$$E_{CB} = E_{fb} - \frac{kT}{e} ln \frac{N_C}{N_D} \tag{6}$$

where k is the Boltzmann constant, T is the absolute temperature, e is the electron charge, N_C is the effective density of states in the CB, and N_D is the effective charge density [108]. Considering that the values of N_D and N_C are similar, the second term in Eq. (6) should be relatively small and then conduction band potential (E_{CB}) can be approximated to E_{fb} [109]. Thus, the relative positions of VB and CB edge potentials of the semiconductors were estimated from E_{bg} and E_{fb} values and using the Eqs. (5, 6), as shown in Fig. 6e. All electrodes show sufficient CB potential values to oxidize H_2O/O_2 (see dashed line in Fig. 6e. The photocatalytic
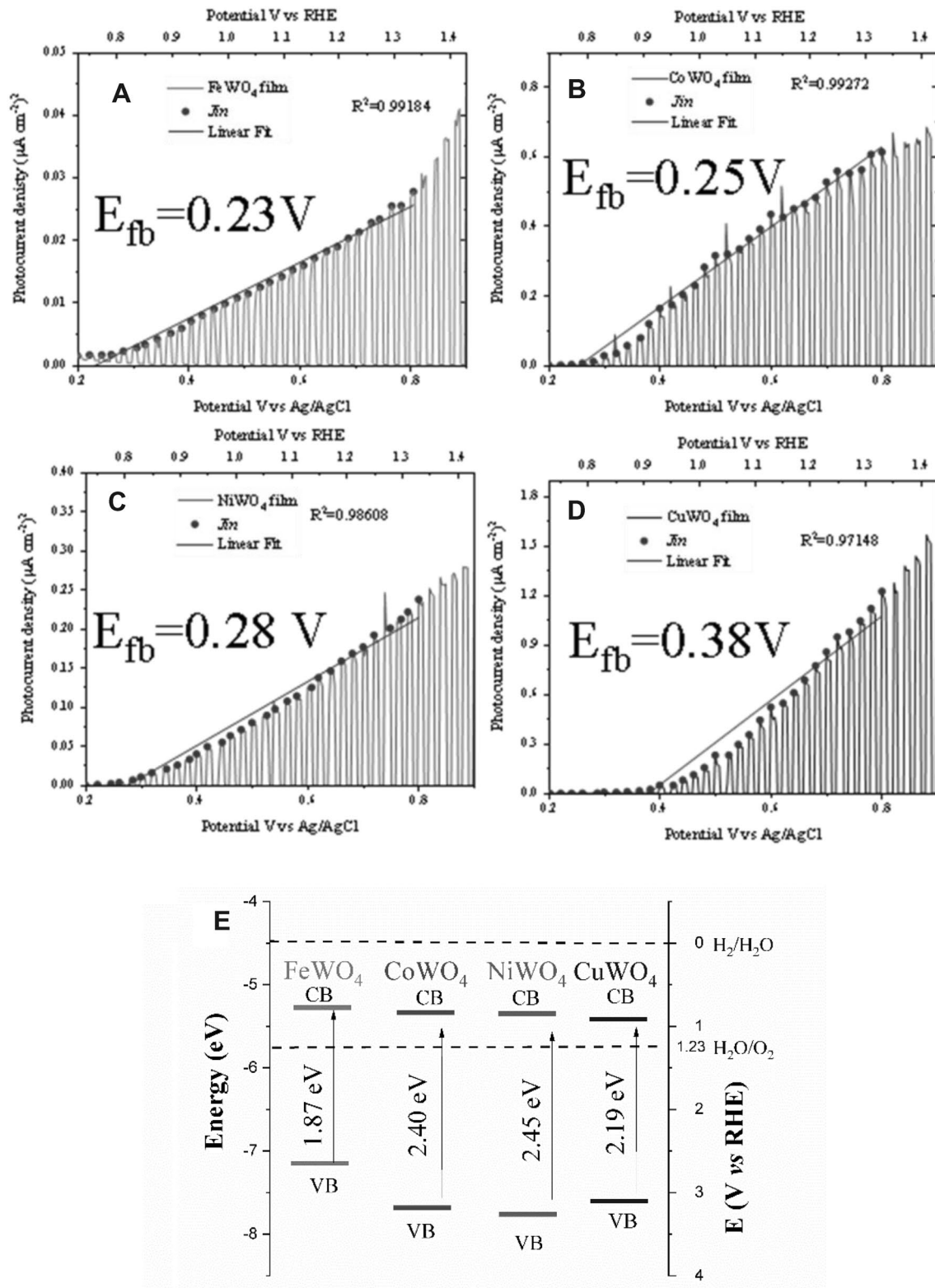
Fig. 6 Variation in the square of the photocurrent density with applied potential, for (a) FeWO$_4$, (b) CoWO$_4$, (c) NiWO$_4$, and (d) CuWO$_4$ electrode in 0.1 mol L^{-1} Na$_2$SO$_4$ aqueous solution, under polychromatic irradiation obeying Butler-Gärtner model and (e) the experimentally determined band diagrams

activity of each material is dependent on the relative positions of the conduction and valence bands. Previous studies reveal that it is important to determine the oxidation potential of species present in solution, relating this potential to the positions of CB and VB to predict the photocatalytic capacity of the semiconductor material [11, 102]. Similarly, E_{fb} values were estimated by Mott-Schottky plot through Electrochemical Impedance Spectroscopy. Fig S5(a) shows the Mott-Schottky curves and relative positions of the CB and VB obtained for all samples. As observed at Fig S5(b), there are no significant differences for the relative positions of the bands for curves obtained by Mott-Schottky or by Butler-Gärtner model.

Figures S6(a–d) display the cyclic voltammetry (CV) curves of AWO_4 (A^{2+} = Fe, Co, Ni, and Cu) films registered at 20 mV s^{-1} in the dark and under polychromatic irradiation. In the dark, the electrodes presented an almost zero capacitive current. As mentioned before, the potential value associated with OER serves to limit the potential window toward anodic reactions. The OCP shifted toward more negative values under irradiation conditions, resulting in a photopotential of − 20, − 60, − 80, and − 50 mV for FeWO$_4$, CoWO$_4$, NiWO$_4$, and CuWO$_4$ photoelectrodes, respectively. These differences recorded in the OPC before and after illumination may be attributed to electron accumulation in the conduction band (CB), due to the electron–hole charge separation [110]. According to theory, after adequate illumination of a n-type semiconductor oxide, the electrons accumulated in the CB are collected by circuit until the Pt counter-electrode, while the photogenerated holes are moved to the electrode/electrolyte interface, thus generating the anodic photocurrent [111]. The photocurrent density of electrodes was respectively 15 µA cm^{-2}, 30 µA cm^{-2}, 20 µA cm^{-2}, and 48 µA cm^{-2} at 1.0 V vs. Ag/AgCl (1.53 V vs. RHE) for FeWO$_4$, CoWO$_4$, NiWO$_4$, and CuWO$_4$ electrodes, as displayed in Figs. S6(a–d). The photoelectrochemical performance of photocatalyst electrodes fabricated in different synthesis methods reported in recent years were compared with this work, as shown in Table S2. Table S2 relating synthesis methods, photocurrent values, type of irradiation and electrolyte was presented [18, 19, 112–125]. Photocurrent values in photoelectrochemical measurements are dependent on several factors, including the material's bandgap energy value, material defects, and the ability of electron charges to reach the conductive substrate. Even with a higher E_{bg} value, CuWO$_4$ film presented higher photocurrent value, indicating that the photogenerated charges reach the conductive substrate more easily than the other AWO_4 investigated.

To investigate the photocurrent stability and e_{CB}^-/h_{VB}^+ recombination lifetime of electrodes in an aqueous medium, a photoelectrochemical study was carried out by measuring the photocurrent density over time at a constant potential of ca. 0.7 V vs. Ag/AgCl (1.23 V vs. RHE). This study is based on transient photocurrent behavior, in which the current response of a system is monitored while a light source is modulated periodically (usually light-on and light-off). Based on this measure, it is possible to study charge carrier dynamics and their traps in a semiconductor material as photoelectrode. The curves registered for AWO_4 films are displayed in Fig. 7. In the dark, all films displayed the current was almost null, while under irradiation, the photocurrent increased abruptly because of charge separation and electrons accumulating in the conduction band, a typical characteristic of n-type semiconductor oxides, as seen in Fig. 7a. In addition, the films demonstrated excellent photo-stability for 2100s, except the FeWO$_4$ film, whose, its photocurrent density has decreased continuously over time. The photocurrent density values followed the same results exposed previously by LSV and cyclic voltammetry measurements, see Fig. 5 and S6.

To obtain the electron–hole recombination lifetimes for the photoelectrodes, photocurrent-time curves, following the schematic representation in Fig. 7b, were analyzed according to Eq. (3). This equation shows that the kinetics of the transient photocurrent can be obtained from slope of the ln R vs. time (t) plot, as shown in Fig. 7c for FeWO$_4$, CoWO$_4$, NiWO$_4$, and CuWO$_4$ photoelectrodes, biased at 0.70 V. The reciprocal $1/\tau$ is related to the electron–hole lifetime. In previous studies, we demonstrated that the mass transport mechanism (i.e. migration or diffusion) in the system does not alter the recombination exponential profile of transient photocurrent utilized to determine the lifetime [102]. As observed in Fig. 7a and schematically represented in Fig. 7b, an initial anodic photocurrent spike J_{in} indicates the injection of electrons in the CB owing to the electron/hole charge separation process. At the same time, electrons are transported to the conductor substrate to be collected by the external circuit; the holes are moved towards the semiconductor surface where they are reduced by the species in the electrolyte. Simultaneously, the photocurrent decreases exponentially with time until it reaches a steady-state photocurrent density (Jst) because of charge recombination.

The slope of the plot provides photocurrent transient (τ), which is related to the charge recombination lifetime in each electrode. The recombination lifetime results are displayed in Table S3. The τ values were calculated at about 83 ± 7, 32 ± 3, 25 ± 4, and 40 ± 1 s for the FeWO$_4$, CoWO$_4$, NiWO$_4$ and CuWO$_4$ films, respectively. These τ values for the CoWO$_4$ and NiWO$_4$ films are smaller than the FeWO$_4$ and CuWO$_4$ films. However, these charge recombination time values are not in agreement with the photocurrent values shown in Fig. 5. Thus, Nyquist plots were used to assess the effective parallel resistance of charge transfer in the samples. Fig S7 shows the Nyquist plots. Even not displaying a well-defined arc as a semicircle, the maximum values observed for the Z' axis were used to verify the greater or lesser
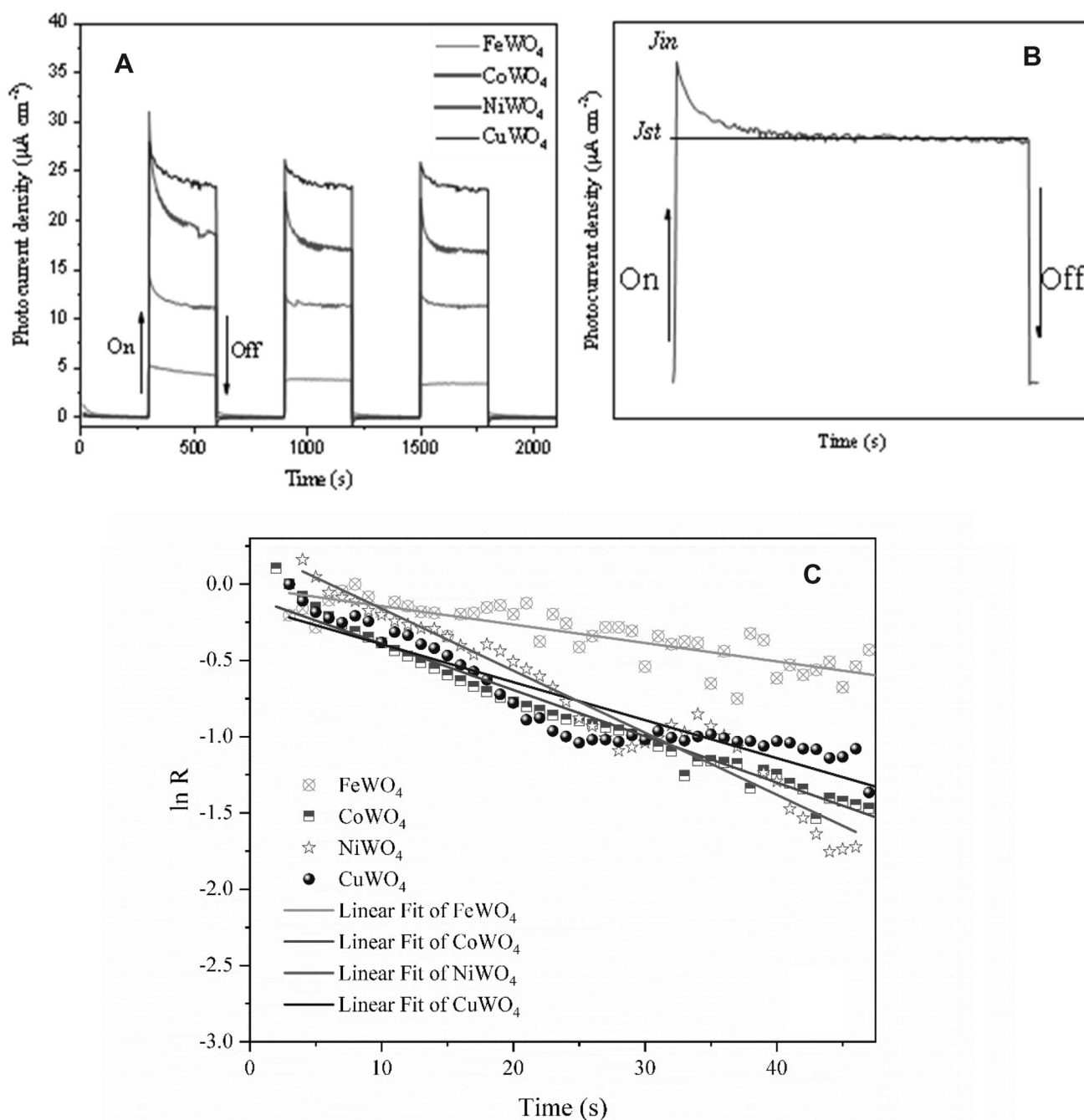
Fig. 7 **a** Photocurrent density-time (*J*-t) curves of the annealed films measured under polychromatic illumination with chopped 300 s light on/off at 0.7 V vs. Ag/AgCl, **b** schematic representation of photocurrent transient curve and **c** normalized plot of current–time dependence for AWO_4 (A^{2+} = Fe,Co, Ni, and Cu)

tendency in charge transfers. The reduction of the effective parallel resistance indicates a better charge transfer for $CuWO_4$, $CoWO_4$, $NiWO_4$, and $FeWO_4$ samples, respectively. This sequence agrees with the photocurrent values. Thus, probably, the electrons promoted to the conduction band do not return to VB. However, we have suppressed defects in the crystal lattice and we believed the holes are captured by traps present in the grain boundaries of the material. Therefore, the photoelectrochemical properties were observed in different wolframite films with anodic photocurrent and capable of harvesting visible light allowing several photoelectrochemical applications.

4 Conclusion

In summary, $FeWO_4$, $CoWO_4$, $NiWO_4$, and $CuWO_4$ thin films onto FTO-glass were synthesized with success by the PPM method via drop-casting after heat treatment at 500 °C for 2 h. XRD patterns analyses confirmed the presence of wolframite-type monoclinic structure for $FeWO_4$, $CoWO_4$, and $NiWO_4$ films, while the $CuWO_4$ film exhibits a triclinic structure. The AWO_4 (A^{2+} = Fe, Co, Ni, and Cu) films showed an ability to absorb in the visible light region, which suggests being excellent harvesters of sunlight for energy conversion applications, such as H_2O oxidation. Morphological features showed by means of FE-SEM images revealed the presence of nanostructured oxides with irregular shapes and the diverse average size of particles. The PEC testing under illumination revealed anodic photocurrent and negative photopotential characteristics of n-type semiconductors oxides. In inert electrolyte, the $CuWO_4$ electrode showed the highest photocurrent density value of 48 μA cm^{-2} at 1.0 V vs. Ag/AgCl (1.53 V vs. RHE). In addition, all electrodes demonstrated excellent chemical stability for photoelectrochemical oxygen evolution reaction with constant bias potential at 0.7 V vs. Ag/AgCl (1.23 V vs. RHE). From E_{bg} and E_{fb} values were possible to assemble a diagram of (CB and VB) positions, which leads to deducting the greatest applicability of electrodes in PEC, exploring these AWO_4 (A^{2+} = Fe, Co, Ni, and Cu) films as electrodes with a high potential to H_2O-splitting photocatalysts.

Declarations

Conflict of interest The authors declare that they have no known competing financial interests or personal relationships that could have appeared to influence the work reported in this paper.

References

1. Kumar P, Saroj DP (2014) Water-energy-pollution nex- us for growing cities. Urban Climate 10:846–853. https://doi.org/10.1016/j.uclim.2014.07.004
2. Bajorowicz B, Kobylański MP, Malankowska A, Mazierski P, Nadolna J, Pieczyńska A, Zaleska-Medynska A (2018) Application of metal oxide-based photocatalysis. In: Zalenska-Medynska A (ed) Metal Oxide-Based Photocatalysis; Fundamentals and Prospects for Application; Metal Oxides, vol series, 1st edn. Elsevier, Amsterdam, pp 211–340
3. van de Krol R, Liang Y, Schoonman J (2008) Solar hydrogen production with nanostructured metal oxides. J Mater Chem 18:2311–2320. https://doi.org/10.1039/B718969A
4. Kalanur S, Hwang J-Y, Seo H (2017) Facile fabrication of bitter-gourd-shaped copper (II) tungstate thin films for improved photocatalytic water splitting. J Catal 350:197–202. https://doi.org/10.1016/j.jcat.2017.04.008
5. Garcia-Segura S, Brillas E (2017) Applied photoelectrocatalysis on the degradation of organic pollutants in wastewaters. J Photochem Photobiol C 31:1–35. https://doi.org/10.1016/j.jphotochemrev.2017.01.005
6. Shinde SS, Bhosale CH, Rajpure KY (2014) Kinetic analysis of heterogeneous photocatalysis: role of hydroxyl radicals. Catal Rev—Sci Eng 55:79–133. https://doi.org/10.1080/01614940.2012.734202
7. Djurišić AB, Leung YH, Ching Ng AM (2014) Strategies for improving the efficiency of semiconductor metal oxide photocatalysis. Mater Horiz 1:400–410. https://doi.org/10.1039/C4MH00031E
8. Peiris S, de Silva HB, Ranasinghe KN, Bandara SV, Perera IR (2021) Recent development and future prospects of TiO_2 photocatalysis. J Chin Chem Soc 68:738–769. https://doi.org/10.1002/jccs.202000465
9. Carvalho IC, Barbosa ML, Costa MJS, Longo E, Cavalcante LS, Viana VGF, Santos, & R.S. (2020) TiO_2-based dye-sensitized solar cells prepared with bixin and norbixin natural dyes: effect of 2,2'-bipyridine additive on the current and voltage. Optik 218:165236–165245. https://doi.org/10.1016/j.ijleo.2020.165236
10. Costa MJS, Costa GS, Lima AEB, da Luz Júnior GE, Longo E, Cavalcante LS, Santos RS (2018) Photocurrent response and progesterone degradation by employing WO_3 films modified with platinum and silver nanoparticles. ChemPlusChem 83:1153–1161. https://doi.org/10.1002/cplu.201800534
11. Costa GS, Costa MJS, Oliveira HG, Lima LCB, Luz GE Jr, Cavalcante LS, Santos RS (2020) Effect of the applied potential condition on the photocatalytic properties of Fe_2O_3|WO_3 heterojunction films. J Inorg Organomet Polym Mater 30:2851–2862. https://doi.org/10.1007/s10904-019-01429-0
12. Qadir AM, Erdogan IY (2019) Structural properties and enhanced photoelectrochemical performance of ZnO films decorated with Cu_2O nanocubes. Int J Hydrogen Energy 44:18694–18702. https://doi.org/10.1016/j.ijhydene.2019.01.101
13. Maruska HP, Ghosh AK (1979) A study of oxide-based heterostructure photoelectrodes. Solar Energ Mater 1:411–429. https://doi.org/10.1016/0165-1633(79)90008-X
14. Su J, Guo L, Bao N, Grimes CA (2011) Nanostructured WO_3/$BiVO_4$ heterojunction films for efficient photoelectrochemical water splitting. Nano Lett 11:1928–1933. https://doi.org/10.1021/nl2000743
15. Kamat PV (1993) Photochemistry on nonreactive and reactive (semiconductor) surfaces. Chem Rev 93:267–300. https://doi.org/10.1021/cr00017a013

16. Sivula K, Formal FL, Grätzel M (2009) WO$_3$−Fe$_2$O$_3$ photoanodes for water splitting: a host scaffold, guest absorber approach. Chem Mater 2:2862–2867. https://doi.org/10.1021/cm900565a

17. Minggu LJ, Daud WRW, Kassim MB (2010) An overview of photocells and photoreactors for photoelectrochemical water splitting. Int J Hydrogen Energy 35:5233–5244. https://doi.org/10.1016/j.ijhydene.2010.02.133

18. Lima AEB, Reis RYN, Ribeiro LS, Ribeiro LK, Assis M, Santos RS, Fernandes CHM, Cavalcante LS, Longo E, Osajima JAO, Luz GE Jr (2021) Microwave-assisted hydrothermal synthesis of CuWO$_4$-palygorskite nanocomposite for enhanced visible photocatalytic response. J Alloy Compd 863:158731–158742. https://doi.org/10.1016/j.jallcom.2021.158731

19. Moura JPC, Reis RYN, Lima AEB, Santos RS, Luz GE Jr (2020) Improved photoelectrocatalytic properties of ZnO/CuWO$_4$ heterojunction film for RhB degradation. Journal of Photochemistry and Photobiology A-Chemistry 401:112778–112783. https://doi.org/10.1016/j.jphotochem.2020.112778

20. García-Pérez UM, Martinez-de la Cruz A, Peral J (2012) Transition metal tungstates synthesized by co-precipitation method: Basic photocatalytic properties. Electrochim Acta 81:227–232. https://doi.org/10.1016/j.electacta.2012.07.045

21. Chen P, He H-Y (2014) H$_2$ evolution from H$_2$O/H$_2$O$_2$/MWO$_4$ (M = Fe^{2+}, Co^{2+}, Ni^{2+}) systems by photocatalytic reaction. Res Chem Intermed 40:1947–1956. https://doi.org/10.1007/s11164-013-1092-5

22. Zawawi SMM, Yahya R, Hassan A, Mahmud HNME, Daud MN (2013) Structural and optical characterization of metal tungstates (MWO$_4$; M=Ni, Ba, Bi) synthesized by a sucrose-templated method. Chem Central J 7:1–10. https://doi.org/10.1186/1752-153X-7-80

23. Ruiz-Fuertes J, Friedrich A, Pellicer-Porres J, Errandonea D, Segura A, Morgenroth W, Haussühl E, Tu C-Y, Polian A (2011) Structure solution of the high-pressure phase of CuWO$_4$ and evolution of the Jahn-Teller distortion. Chem Mater 23:4220–4226. https://doi.org/10.1021/cm201592h

24. Ke J, Younis MA, Kong Y, Zhou H, Liu J, Lei L, Hou Y (2018) Nanostructured ternary metal tungstate-based photocatalysts for environmental purification and solar water splitting: a review. Nano-Micro Letters 10:69. https://doi.org/10.1007/s40820-018-0222-4

25. Errandonea D, Ruiz-Fuertes J (2018) A brief review of the effects of pressure on wolframite-type oxides. Crystals 8:71. https://doi.org/10.3390/cryst8020071

26. Gao J, Gao Y, Sui Z, Dong Z (2018) Hydrothermal synthesis of BiOBr/FeWO$_4$ composite photocatalysts and their photocatalytic degradation of doxycycline. J Alloy Compd 732:43–51. https://doi.org/10.1016/j.jallcom.2017.10.092

27. Gao Q, Liu Z (2017) FeWO$_4$ nanorods with excellent UV–visible light photocatalysis. Prog Nat Sci: Mater Int 27:556–560. https://doi.org/10.1016/j.pnsc.2017.08.016

28. Mahendran N, Udayakumar S, Praveen K (2019) pH-Controlled photocatalytic abatement of RhB by an FeWO$_4$/BiPO$_4$ p–n heterojunction under visible light irradiation. New J Chem 43:17241–17250. https://doi.org/10.1039/C9NJ04263F

29. Shanmugapriya S, Surendran S, Nithya VD, Saravanan P, Selvan RK (2016) Temperature dependent electrical and magnetic properties of CoWO$_4$ nanoparticles synthesized by sonochemical method. Mater Sci Eng B 214:57–67. https://doi.org/10.1016/j.mseb.2016.09.002

30. Pandey PK, Bhave NS, Kharat RB (2006) Structural, optical, electrical and photovoltaic electrochemical characterization of spray deposited NiWO$_4$ thin films. Electrochim Acta 51:4659–4664. https://doi.org/10.1016/j.electacta.2005.12.042

31. Song Z, Ma J, Sun H, Wang W, Sun Y, Sun L, Liu Z, Gao C (2009) Synthesis of NiWO$_4$ nano-particles in low-temperature molten salt medium. Ceram Int 35:2675–2678. https://doi.org/10.1016/j.ceramint.2009.03.010

32. AlShehri SM, Ahmed J, Alzahrani AM, Ahamad T (2017) Synthesis, characterization, and enhanced photocatalytic properties of NiWO$_4$ nanobricks. New J Chem 41:8178–8186. https://doi.org/10.1039/C7NJ02085F

33. Karthiga R, Kavitha B, Rajarajan M, Suganthi A (2015) Photocatalytic and antimicrobial activity of NiWO$_4$ nanoparticles stabilized by the plant extract. Mater Sci Semicond Process 40:123–129. https://doi.org/10.1016/j.mssp.2015.05.037

34. Srirapu VKV, Kumar PA, Srivastava P, Singh RN, Sinha ASK (2016) Nanosized CoWO$_4$ and NiWO$_4$ as efficient oxygen-evolving electrocatalysts. Electrochiimica Acta 209:75–84. https://doi.org/10.1016/j.electacta.2016.05.042

35. Gaillard N, Chang Y, DeAngelis A, Higgins S, Braun A (2013) A nanocomposite photoelectrode made of 2.2 eV band gap copper tungstate (CuWO$_4$) and multi-wall carbon nanotubes for solar-assisted water splitting. Int J Hydrog Energ 38:3166–3176. https://doi.org/10.1016/j.ijhydene.2012.12.104

36. Shekofteh-Gohari M, Habibi-Yangjeh A (2016) Fabrication of novel magnetically separable visible-light-driven photocatalysts through photosensitization of Fe$_3$O$_4$/ZnO with CuWO$_4$. J Ind Eng Chem 44:174–184. https://doi.org/10.1016/j.jiec.2016.08.028

37. Lima AEB, Costa MJS, Santos RS, Batista NC, Cavalcante LS, Longo E, Luz GE Jr (2017) Facile preparation of CuWO$_4$ porous films and their photoelectrochemical properties. Electrochim Acta 256:139–145. https://doi.org/10.1016/j.electacta.2017.10.010

38. Ding W, Wu X, Lu Q (2019) Structure and photocatalytic activity of thin-walled CuWO$_4$ nanotubes: an experimental and DFT study. Mater Lett 253:323–326. https://doi.org/10.1016/j.matlet.2019.06.109

39. Mohanty B, Naik KK, Sahoo S, Jena B, Chakraborty B, Rout CS, Jena BK (2018) Efficient photoelectrocatalytic activity of CuWO$_4$ nanoplates towards the oxidation of NADH driven in visible light. ChemistrySelect 3:9008–9012. https://doi.org/10.1002/slct.201801137

40. Zhou M, Liu Z, Li X, Liu Z (2018) Promising three-dimensional flowerlike CuWO$_4$ photoanode modified with CdS and FeOOH for efficient photoelectrochemical water splitting. Ind Eng Chem Res 57:6210–6217. https://doi.org/10.1021/acs.iecr.8b00358

41. Lalić MV, Popović ZS, Vukajlović FR (2012) Electronic structure and optical properties of CuWO$_4$: AN ab initio study. Comput Mater Sci 63:163–167. https://doi.org/10.1016/j.commatsci.2012.05.074

42. Gonzalez CM, Du X, Dunford JL, Post ML (2012) Copper tungstate thin-films for nitric oxide sensing. Sens Actuators, B Chem 173:169–176. https://doi.org/10.1016/j.snb.2012.06.067

43. Poovaragan S, Sundaram R, Magdalane CM, Kaviyarasu K, Maaza M (2019) Photocatalytic activity and humidity sensor studies of magnetically reusable FeWO$_4$–WO$_3$ composite nanoparticles. J Nanosci Nanotechnol 19:859–866. https://doi.org/10.1166/jnn.2019.15565

44. Lannelongue P, Le Vot S, Fontaine O, Brousse T, Favier F (2019) Electrochemical study of asymmetric aqueous supercapacitors based on high density oxides: C/Ba$_{0.5}$Sr$_{0.5}$Co$_{0.8}$Fe$_{0.2}$O$_{3-δ}$ and FeWO$_4$/Ba$_{0.5}$Sr$_{0.5}$Co$_{0.8}$Fe$_{0.2}$O$_{3-δ}$. Electrochimica Acta. 326:134886. https://doi.org/10.1016/j.electacta.2019.134886

45. Kumar RD, Karuppuchamy S (2014) Microwave-assisted synthesis of copper tungstate nanopowder for supercapacitor applications. Ceram Int 40:12397–12402. https://doi.org/10.1016/j.ceramint.2014.04.090

46. Kumar RD, Karuppuchamy S (2016) Microwave mediated synthesis of nanostructured Co–WO$_3$ and CoWO$_4$ for supercapacitor

applications. J Alloy Compd 674:384–391. https://doi.org/10.1016/j.jallcom.2016.03.074

47. Li CL, Fu ZW (2008) Nano-sized copper tungstate thin films as positive electrodes for rechargeable Li batteries. Electrochim Acta 53:4293–4301. https://doi.org/10.1016/j.electacta.2008.01.014

48. Liu J, Zhang Z, Wang Z, Tang M, Li J, Yi J, Zuo T, Wu Y, Ma Q (2017) Flower-like WO$_3$/CoWO$_4$/Co nanostructures as high performance anode for lithium ion batteries. J Alloy Compd 727:107–113. https://doi.org/10.1016/j.jallcom.2017.08.057

49. Peng T, Liu C, Hou X, Zhang Z, Wang C, Yan H, Lu Y, Liu X, Luo Y (2017) Control growth of mesoporous nickel tungstate nanofiber and its application as anode material for lithium-ion batteries. Electrochim Acta 224:460–467. https://doi.org/10.1016/j.electacta.2016.11.154

50. Thongpan W, Louloudakis D, Pooseekheaw P, Kumpika T, Kantarak E, Sroila W, Panthawan A, Thongsuwan W, Singjai P (2019) Porous CuWO$_4$/WO$_3$ composite films with improved electrochromic properties prepared by sparking method. Mater Lett 257:126747. https://doi.org/10.1016/j.matlet.2019.126747

51. Tang Y, Rong N, Liu F, Chu M, Dong H, Zhang Y, Xiao P (2016) Enhancement of the photoelectrochemical performance of CuWO$_4$ films for water splitting by hydrogen treatment. Appl Surf Sci 361:133–140. https://doi.org/10.1016/j.apsusc.2015.11.129

52. Hu D, Diao P, Xu D, Xia M, Gu Y, Wu Q, Li C, Yang S (2016) Copper(II) tungstate nanoflake array films: sacrificial template synthesis, hydrogen treatment, and their application as photoanodes in solar water splitting. Nanoscale 8:5892–5901. https://doi.org/10.1039/C5NR09210H

53. Abdul-hamead AA, Salman ZA, Othman FM (2019) Synthesis and characterization of Iron tungstate oxide films by advanced controlled spray pyrolysis technique. Iraqi J Phys 17:29–39. https://doi.org/10.20723/ijp.17.41.29-39

54. Yourey JE, Bartlett BM (2011) Electrochemical deposition and photoelectrochemistry of CuWO$_4$, a promising photoanode for wateroxidation. J Mater Chem 21:7651–7660. https://doi.org/10.1039/C1JM11259G

55. Gouveia AF, Vieira VEM, Sczancoski JC, Lemos PS, Rout SK, Arul NS, Longo E, Cavalcante LS (2020) Electronic structure, morphological aspects, and photocatalytic discoloration of three organic dyes with MgWO$_4$ powders synthesized by the complex polymerization method. J Inorg Organomet Polym Mater 30(2020):2952–2970. https://doi.org/10.1007/s10904-019-01435-2

56. Benchikhi M, Ouatib RE, Guillemet-Fritsch S, Er-Rakho L, Durand B (2017) Investigation of structural transition in molybdates CuMo$_{1-x}$W$_x$O$_4$ prepared by polymeric precursor method. Processing and Application of Ceramics 11:21–26. https://doi.org/10.2298/PAC1701021B

57. Dimesso L (2016) Pechini processes: an alternate approach of the sol–gel method, preparation, properties, and applications. In: Klein L, Aparicio M, Jitianu A (eds) Handbook of sol-gel science and technology. Springer, Cham. https://doi.org/10.1007/978-3-319-19454-7_123-1

58. Kakihana M (1996) Invited review "sol-gel" preparation of high temperature superconducting oxides. J Sol-Gel Sci Technol 6:7–55. https://doi.org/10.1007/BF00402588

59. Maurera MAMA, Souza AG, Soledade LEB, Pontes FM, Longo E, Leite ER, Varela JA (2004) Microstructural and optical characterization of CaWO$_4$ and SrWO$_4$ thin films prepared by a chemical solution method. Mater Lett 58:727–732. https://doi.org/10.1016/j.matlet.2003.07.002

60. Cavalcante LS, Sczancoski JC, Albarici VC, Matos JME, Varela JA (2008) Synthesis, characterization, structural refinement and

61. optical absorption behavior of PbWO$_4$ powders. Mater Sci Eng B 150:18–25. https://doi.org/10.1016/j.mseb.2008.02.003

61. Tauc J (1968) Optical properties and electronic structure of amorphous Ge and Si. Mater Res Bull 3:37–46. https://doi.org/10.1016/0025-5408(68)90023-8

62. Resende ALS, Costa AGR, Lima AEB, Costa MJS, Longo E, Cavalcante LS, Santos RS (2020) An investigation of photovoltaic devices based on p-type Cu$_2$O and n-type γ-WO$_3$ junction through an electrolyte solution containing a redox pair. Int J Energy Res 45:2797–2809. https://doi.org/10.1002/er.5974

63. Gärtner WW (1959) Depletion-layer photoeffects in semiconductors. Phys Rev 116:84–87. https://doi.org/10.1103/PhysRev.116.84

64. Butler MA (1977) Photoelectrolysis and physical properties of the semiconducting electrode WO$_2$. J Appl Phys 48:1914–1920. https://doi.org/10.1063/1.323948

65. Yang W, Prabhakar RR, Tan J, Tilley SD, Moon J (2019) Strategies for enhancing the photocurrent, photovoltage, and stability of photoelectrodes for photoelectrochemical water splitting. Chem Soc Rev 48:4979–5015. https://doi.org/10.1039/C8CS00997J

66. Bard AJ, Faulkener LR (2001) Electrochemical methods: fundamentals and applications, 2nd edn. Wiley, New Jersey, p 54

67. Dholam R, Patel N, Santini A, Miotello A (2010) Efficient indium tin oxide/Cr-doped-TiO$_2$ multilayer thin films for H$_2$ production by photocatalytic water-splitting. Int J Hydrogen Energy 35:9581–9590. https://doi.org/10.1016/j.ijhydene.2010.06.097

68. Spadavecchia F, Ardizzone S, Cappelletti G, Falciola L, Ceotto M, Lotti D (2013) Investigation and optimization of photocurrent transient measurements on nano-TiO$_2$. J Appl Electrochem 43:217–225. https://doi.org/10.1007/s10800-012-0485-2

69. Escobar C, Cid-Dresdner H, Kittl P, Duemler I (1971) The Relation between "light wolframite" and common wolframite. Am Miner 56:489–498

70. Weitzel H (1976) Kristallstrukturverfeinerung von Wolframiten und Columbiten. Z Kristallogr 144:238–258. https://doi.org/10.1524/zkri.1976.144.16.238

71. Kihlborg L, Gebert E (1970) CuWO$_4$, a distorted wolframite-type structure. Acta Crystallogr Sect B: Struct Crystallogr Cryst Chem 26:1020–1026. https://doi.org/10.1107/S0567740870003515

72. Yu F, Cao L, Huang J, Wu J (2013) Effects of pH on the microstructures and optical property of FeWO$_4$ nanocrystallites prepared via hydrothermal method. Ceram Int 39:4133–4138. https://doi.org/10.1016/j.ceramint.2012.10.269

73. Innocenzi P, Malfatti L (2013) Mesoporous thin films: properties and applications. Chem Soc Rev 42:4198–4216. https://doi.org/10.1039/C3CS35377J

74. Wilber. Image Manipulation Program. *Gimp—GNU* (Version 2.10.30) 21 Dec 2021. https://www.gimp.org/news/2021/12/21/gimp-2-10-30-released/

75. Kwong WL, Savvides N, Sorrell CC (2012) Electrodeposited nanostructured WO$_3$ thin films for photoelectrochemical applications. Electrochim Acta 75:371–380. https://doi.org/10.1016/j.electacta.2012.05.019

76. Zhang J, Wang Y, Li S, Wang X, Huang F, Xie A, Shen Y (2011) Controlled synthesis, growth mechanism and optical properties of FeWO$_4$ hierarchical microstructures. Cryst Eng Commun 13:5744–5750. https://doi.org/10.1039/C1CE05416C

77. Ejima T, Banse T, Takatsuka H, Kondo Y, Ishino M, Kimura N, Watanabe M, Matsubara I (2006) Microscopic optical and photoelectron measurements of MWO$_4$ (M=Mn, Fe, and Ni). J Lumines 119:59–63. https://doi.org/10.1016/j.jlumin.2005.12.012

78. Ling C, Zhou LQ, Jia H (2014) First-principles study of crystalline $CoWO_4$ as oxygen evolution reaction catalyst. RSC Adv 4:24692–24697. https://doi.org/10.1039/C4RA03893B

79. Bharati R, Singh RA, Wanklyn BM (1981) On electrical transport in $CoWO_4$ single crystals. J Mater Sci 16:775–779. https://doi.org/10.1007/BF02402795

80. Tian CM, Jiang M, Tang D, Qiao L, Xiao HY, Oropeza FE, Hofmann JP, Hensen EJM, Tadich A, Li W, Qi DC, Zhang KHL (2019) Elucidating the electronic structure of $CuWO_4$ thin films for enhanced photoelectrochemical water splitting. J Mater Chem A 7:11895–11907. https://doi.org/10.1039/C8TA12070F

81. Ojha DP, Karki HP, Song J, Kim HJ (2018) Decoration of g-C_3N_4 with hydrothermally synthesized $FeWO_4$ nanorods as the high-performance supercapacitors. Chem Phys Lett 712:83–88. https://doi.org/10.1016/j.cplett.2018.09.070

82. Rajagopal S, Khyzhun OY, Djaoued Y, Robichaud J, Mangalaraj D (2010) Hydrothermal synthesis and electronic properties of $FeWO_4$ and $CoWO_4$ nanostructures. J Alloy Compd 493:340–345. https://doi.org/10.1016/j.jallcom.2009.12.099

83. Zhu J, Li W, Li J, Li Y, Hu H, Yang Y (2013) Photoelectrochemical activity of $NiWO_4$/WO_3 heterojunction photoanode under visible light irradiation. Electrochim Acta 112:191–198. https://doi.org/10.1016/j.electacta.2013.08.146

84. Wang H, Wang C, Cui X, Qina L, Ding R, Wang L, Liu Z, Zheng Z, Lv B (2018) Design and facile one-step synthesis of $FeWO_4$/Fe_2O_3 di-modified WO_3 with super high photocatalytic activity toward degradation of quasi-phenothiazine dyes. Appl Catal B 221:169–178. https://doi.org/10.1016/j.apcatb.2017.09.011

85. Dadigala R, Bandi R, Gangapuram BR, Guttena V (2019) Construction of in situ self-assembled $FeWO_4$/g-C_3N_4 nanosheet heterostructured Z-scheme photocatalysts for enhanced photocatalytic degradation of rhodamine B and tetracycline. Nanoscale Advances 1:322–333. https://doi.org/10.1039/C8NA00041G

86. Sadiq MMJ, Shenoy US, Bhat DK (2017) Enhanced photocatalytic performance of N-doped RGO-$FeWO_4$/Fe_3O_4 ternary nanocomposite in environmental applications. Mater Today Chem 4:133–141. https://doi.org/10.1016/j.mtchem.2017.04.003

87. Chen S, Yang G, Jia Y, Zheng H (2016) Facile synthesis of $CoWO_4$ nanosheet arrays grown on nickel foam substrates for asymmetric supercapacitors. ChemElectroChem 3:1490–1496. https://doi.org/10.1002/celc.201600316

88. Luo F, Xu R, Ma S, Zhang Q, Hu H, Qu K, Xiao S, Yang Z, Cai W (2019) Engineering oxygen vacancies of cobalt tungstate nanoparticles enable efficient water splitting in alkaline medium. Appl Catal B: Environ 259:118090. https://doi.org/10.1016/j.apcatb.2019.118090

89. Chen S, Yang G, Jia Y, Zheng H (2017) Three-dimensional $NiCo_2O_4$@$NiWO_4$ core–shell nanowire arrays for high performance supercapacitors. J Mater Chem A 5:1028–1034. https://doi.org/10.1039/C6TA08578D

90. Nesbitt HW, Legrand D, Bancroft GM (2000) Interpretation of Ni2p XPS spectra of Ni conductors and Ni insulators. Phys Chem Miner 27:357–366. https://doi.org/10.1007/s002690050265

91. McIntyre S, Cook MG (1975) X-ray photoelectron studies on some oxides and hydroxides of cobalt, nickel, and copper. Anal Chem 47:2208–2213. https://doi.org/10.1021/ac60363a034

92. Dong H, Li Y, Gao D, Zhou M, Hu X, Peng H, Yang L, He J, Zhang Y, Xiao P (2019) Efficient self-assembly solvothermal synthesis of octahedral $CuWO_4$ microstructures assisted by ethylene glycol. J Alloy Compd 785:660–668. https://doi.org/10.1016/j.jallcom.2019.01.224

93. Signorelli AJ, Hayes RG (1973) X-Ray photoelectron spectroscopy of various core levels of lanthanide ions: the roles of monopole excitation and electrostatic coupling. Phys Rev B 8:81–86. https://doi.org/10.1103/PhysRevB.8.81

94. Cao X, Chen Y, Jiao S, Fang Z, Xu M, Liu X, Li L, Pang G, Feng S (2014) Magnetic photocatalysts with a p–n junction: Fe_3O_4 nanoparticle and $FeWO_4$ nanowire heterostructures. Nanoscale 6:12366–12370. https://doi.org/10.1039/C4NR03729D

95. Liu Z, Song Q, Zhou M, Guo Z, Kang J, Yan H (2019) Synergistic enhancement of charge management and surface reaction kinetics by spatially separated cocatalysts and p–n heterojunctions in Pt/$CuWO_4$/Co_3O_4 photoanode. Chem Eng J 374:554–563. https://doi.org/10.1016/j.cej.2019.05.191

96. Yang J, Li C, Diao P (2019) Molybdenum doped $CuWO_4$ nanoflake array films as an efficient photoanode for solar water splitting. Electrochim Acta 308:195–205. https://doi.org/10.1016/j.electacta.2019.04.044

97. Liu L, Mei Z, Tang A, Azarov A, Kuznetsov A, Xue QK, Du X (2016) Oxygen vacancies: the origin of n-type conductivity in ZnO. Phys Rev B 93:235305. https://doi.org/10.1103/physrevb.93.235305

98. Oliveira HG, Ferreira LH, Bertazzoli R, Longo C (2015) Remediation of 17-α-ethinylestradiol aqueous solution by photocatalysis and electrochemically-assisted photocatalysis using TiO_2 and TiO_2/WO_3 electrodes irradiated by a solar simulator. Water Res 72:305–314. https://doi.org/10.1016/j.watres.2014.08.042

99. Lim Y-F, Chua CS, Lee CJJ, Chi D (2014) Sol–gel deposited Cu_2O and CuO thin films for photocatalytic water splitting. Phys Chem Chem Phys 16:25928–25934. https://doi.org/10.1039/C4CP03241A

100. Xiong X, Fan L, Chen G, Wang Y, Wu C, Chen D, Lin Y, Li T, Fu S, Ren S (2019) Boosting water oxidation performance of $CuWO_4$ photoanode by surface modification of nickel phosphate. Electrochim Acta 328:135125. https://doi.org/10.1016/j.electacta.2019.135125

101. Hankin A, Bedoya-Lora FE, Alexander JC, Regoutz A, Kelsall GH (2019) Flat band potential determination: avoiding the pitfalls. J Mater Chem A 7:26162–26176. https://doi.org/10.1039/C9TA09569A

102. Costa MJS, Costa GS, Lima AEB, Luz GE Jr, Longo E, Cavalcante LS, Santos RS (2018) Investigation of charge recombination lifetime in γ-WO_3 films modified with Ag^0 and Pt^0 nanoparticles and its influence on photocurrent density. Ionics 24:3291–3297. https://doi.org/10.1007/s11581-018-2640-1

103. Radecka M, Rekas M, Trenczek-Zajac A, Zakrzewska K (2008) Importance of the band gap energy and flat band potential for application of modified TiO_2 photoanodes in water photolysis. J Power Sour 181:46–55. https://doi.org/10.1016/j.jpowsour.2007.10.082

104. Bak T, Nowotny J, Rekas M, Sorrell CC (2002) Photo-electrochemical hydrogen generation from water using solar energy. Materials-related aspects. Int J Hydrog Energ 27:991–1021. https://doi.org/10.1016/S0360-3199(02)00022-8

105. Liu Y, Li J, Li W, He H, Yang Y, Li Y, Chen Q (2016) Electrochemical doping induced in situ homo-species for enhanced photoelectrochemical performance on WO_3 nanoparticles film photoelectrodes. Electrochim Acta 210:251–260. https://doi.org/10.1016/j.electacta.2016.05.165

106. Shrestha NK, Schmuki P (2013) Electrochemistry at TiO_2 nanotubes and other semiconductor nanostructures. Electrochemistry 12:87–131. https://doi.org/10.1039/9781849737333-00087

107. Alpuche-Aviles MA, Wu Y (2009) Photoelectrochemical study of the band structure of Zn_2SnO_4 prepared by the hydrothermal method. J Am Chem Soc 131:3216–3224. https://doi.org/10.1021/ja806719x

108. Paulauskas IE, Katz JE, Jellison GE Jr, Lewis NS, Boatner LA, Brown GM (2009) Growth, characterization, and electrochemical properties of doped n-type $KTaO_3$ photoanodes. J Electrochem Soc 156:B580–B587. https://doi.org/10.1149/1.3089281

109. Chen H, Leng W, Xu Y (2014) Enhanced visible-light photoactivity of $CuWO_4$ through a surface-deposited CuO. J Phys Chem C 118:9982–9989. https://doi.org/10.1021/jp502616h

110. Linsebigler AL, Lu G, Yates JT Jr (1995) Photocatalysis on TiO_2 surfaces: principles, mechanisms, and selected results. Chem Rev 95:735–758. https://doi.org/10.1021/cr00035a013

111. Hagfeldt A, Graetzel M (1995) Light-induced redox reactions in nanocrystalline systems. Chem Rev 95:49–68. https://doi.org/10.1021/cr00033a003

112. Polo A, Nomellini C, Grigioni I, Dozzi MV, Selli E (2020) Effective visible light exploitation by copper molybdo-tungstate photoanode. ACS Appl Energ Mater 3:6956–6964. https://doi.org/10.1021/acsaem.0c01021

113. Duan X, Xu C, El Nahrawy AMJ, Chen Z, Zhu J, Wang Q, Liang F. Cao (2022) Ultrasonic spray pyrolysis-assisted fabrication of ultrathin $CuWO_4$ films with improved photoelectrochemical performance. ChemNanoMat 8:e202100419. https://doi.org/10.1002/cnma.202100419

114. Lima AEB, Assis M, Resende ALS, Santos HLS, Mascaro LH, Longo E, Santos RS, Cavalcante LS, Luz GE Jr (2022) $CuWO_4|MnWO_4$ heterojunction thin film with improved photoelectrochemical and photocatalytic properties using simulated solar irradiation. J Solid State Electrochem 26:997–1011. https://doi.org/10.1007/s10008-022-05143-9

115. Chidambaram S, Ramachandran K, Gaidi M, Daoudi K, Natarajamoorthy M (2021) Solution combustion synthesis of iron tungstate nanoparticles for photoelectrochemical water splitting towards oxygen evolution. J Mater Sci: Mater Electron 33:9134–9143. https://doi.org/10.1007/s10854-021-07146-0

116. Rosa WS, Rabelo LG, Zampaulo LGT, Gonçalves RV (2022) Ternary oxide $CuWO_4/BiVO_4/FeCoO_x$ films for photoelectrochemical water oxidation: insights into the electronic structure and interfacial band alignment. ACS Appl Mater Interfaces 14(20):22858–22869. https://doi.org/10.1021/acsami.1c21001

117. Chatterjee P, Chakraborty AK (2022) Enhanced solar water oxidation by $CoWO_4–WO_3$ heterojunction photoanode. Sol Energ 232:312–319. https://doi.org/10.1016/j.solener.2021.12.075

118. Cho HE, Yun G, Arunachalam M, Ahn KS, Kim CS, Lim D-H, Kang SH (2018) Nanolayered $CuWO_4$ decoration on fluorine-doped SnO_2 inverse opals for solar water oxidation. J Electrochem Sci Technol 9:282–291. https://doi.org/10.5229/JECST.2018.9.4.282

119. Zhang Y, Wang L, Xu X (2021) A bias-free $CuBi_2O_4–CuWO_4$ tandem cell for solar-driven water splitting. Inorg Chem Front 8:3863–3870. https://doi.org/10.1039/D1QI00088H

120. Ahmed MI, Adam A, Khan A, Rehman AU, Qamaruddin M, Siddiqui MN, Qamar M (2016) Improved photoelectrochemical water oxidation under visible light with mesoporous $CoWO_4$. Mater Lett 183:281–284. https://doi.org/10.1016/j.matlet.2016.07.137

121. Babu ES, Rani BJ, Ravi G, Yuvakkumar R, Guduru RK, Ganesh V, Kim S (2018) Novel $NiWO_4$ nanoberries morphology effect on photoelectrochemical properties. Mater Lett 220:209–212. https://doi.org/10.1016/j.matlet.2018.03.018

122. Ahmed MI, Adam A, Khan A, Siddiqui MN, Yamani Z, Qamar HM (2016) Synthesis of mesoporous $NiWO_4$ nanocrystals for enhanced photoelectrochemical water oxidation. Mater Lett 177:135–138. https://doi.org/10.1016/j.matlet.2016.04.143

123. Sun Y, Du F, Xie D, Yang D, Jiao Y, Jia L, Fan H (2020) Improved water oxidation via Fe doping of $CuWO_4$ photoanodes: influence of the Fe source and concentration. Chinese Phys B 29:127801. https://doi.org/10.1088/1674-1056/aba9cb

124. Chen Z, Löber M, Rokicińska A, Ma Z, Chen J, Kuśtrowski P, Meyer H-J, Dronskowski R, Slabon A (2020) Increased photocurrent of $CuWO_4$ photoanodes by modification with the oxide carbodiimide $Sn_2O(NCN)$. Dalton Trans 49:3450–3456. https://doi.org/10.1039/C9DT04752B

125. Balasubramanian V, Kannan S, Thangaraj NS, Sivakumar G, Mohanraj K (2020) Role of W-Rich $CuWO_4$ and Doped Zn–$CuWO_4$ ceramics and its improved photoelectrochemical cell performances synthesized by solid state reaction method. ChemistrySelect 5:8959–8968. https://doi.org/10.1002/slct.202000229